iScience

CellPress
OPEN ACCESS

Article

Ebola and Marburg virus VP35 coiled-coil validated as antiviral target by tripartite split-GFP complementation

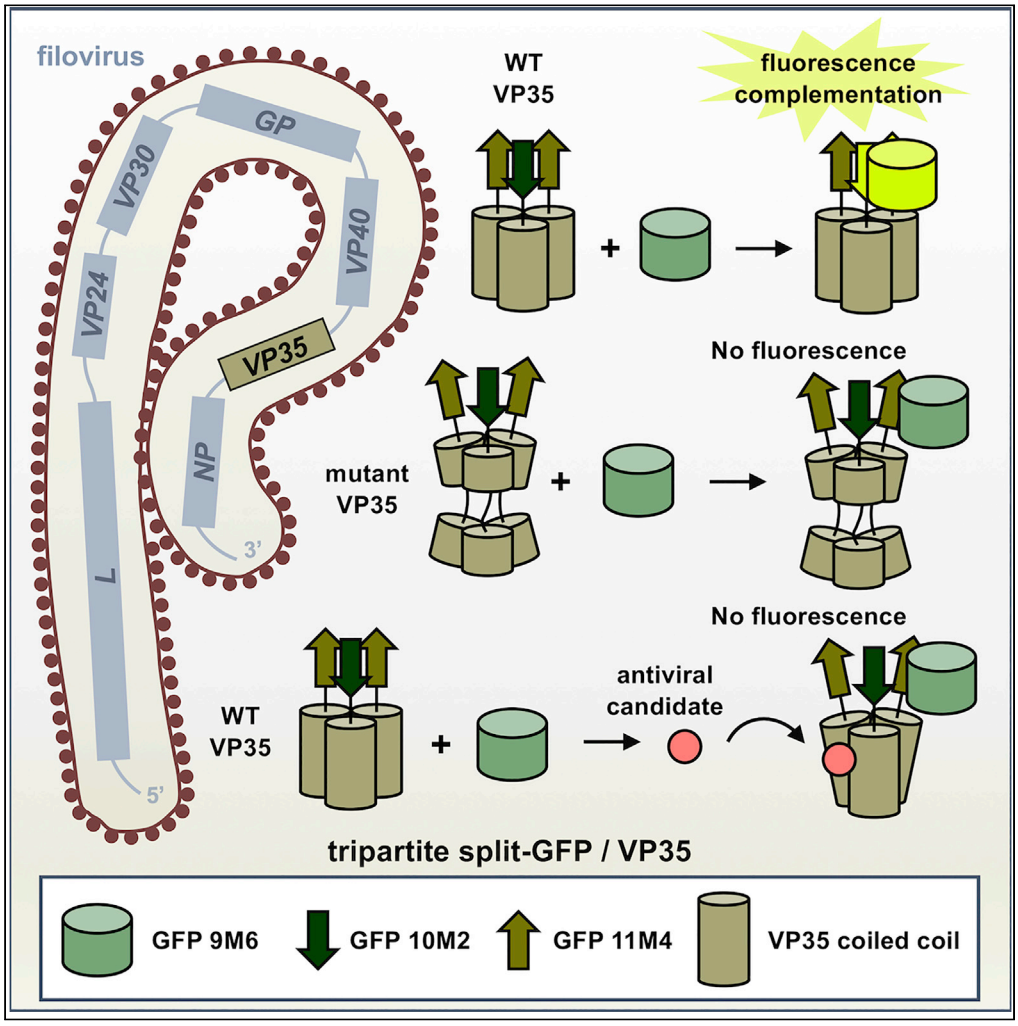

Luca Zinzula, Angela Maria Mereu, Massimiliano Orsini, Christine Seeleitner, Andreas Bracher, István Nagy, Wolfgang Baumeister

zinzula@biochem.mpg.de (L.Z.)
baumeist@biochem.mpg.de (W.B.)

Highlights

Ebola and Marburg virus VP35 oligomerize via trimeric and tetrameric coiled-coil

VP35 coiled-coil assembly triggers fluorescence of a tripartite split-GFP system

Mutations perturbing VP35 coiled-coil hamper split-GFP complementation

Myricetin and TBBT inhibit split-GFP complementation mediated by VP35 coiled-coil

Zinzula et al., iScience 25, 105354
November 18, 2022
https://doi.org/10.1016/j.isci.2022.105354

iScience

CellPress
OPEN ACCESS

Article

Ebola and Marburg virus VP35 coiled-coil validated as antiviral target by tripartite split-GFP complementation

Luca Zinzula,[1,4,*] Angela Maria Mereu,[1] Massimiliano Orsini,[2] Christine Seeleitner,[1] Andreas Bracher,[3] István Nagy,[1] and Wolfgang Baumeister[1,*]

SUMMARY

Ebola virus (EBOV) and Marburg virus (MARV) are highly pathogenic viruses in humans, against which approved antivirals are lacking. During EBOV and MARV infection, coiled-coil mediated oligomerization is essential for the virion protein 35 (VP35) polymerase co-factor function and type I interferon antagonism, making VP35 coiled-coil an elective drug target. We established a tripartite split-green fluorescent protein (GFP) fluorescence complementation (FC) system based on recombinant GFP-tagged EBOV and MARV VP35, which probes VP35 coiled-coil assembly by monitoring fluorescence on *E. coli* colonies, or *in vitro* in 96/384-multiwell. Oligomerization-defective VP35 mutants showed that correct coiled-coil knobs-into-holes pairing within VP35 oligomer is pre-requisite for GFP tags and GFP detector to reconstitute fluorescing full-length GFP. The method was validated by screening a small compound library, which identified Myricetin and 4,5,6,7-Tetrabromobenzotriazole as inhibitors of EBOV and MARV VP35 oligomerization-dependent FC with low-micromolar IC_{50} values. These findings substantiate the VP35 coiled-coil value as antiviral target.

INTRODUCTION

Ebola virus (EBOV, *Zaire ebolavirus* species) and Marburg virus (MARV, *Marburg marburgvirus* species) are the two prototypical members of the *Filoviridae* family of the order *Mononegavirales*, which comprises six recognized genera (namely *Cuevavirus, Dianlovirus, Ebolavirus*, *Marburgvirus*, *Striavirus*, and *Thamnovirus*) whose species possess a characteristic filamentous-shaped virion and genetic organization of single-stranded, non-segmented, negative-sensed RNA genome (Kuhn et al., 2019). EBOV and MARV are highly pathogenic in humans and non-human primates, causing an often fatal disease with up to 90% lethality. While having been sporadic over the past decades and confined to remote rural areas of the Sub-Saharan Africa, EBOV and MARV human outbreaks have in recent years increased in frequency and number of cases, expanded geographically and extended in duration (Languon and Quaye, 2019). Exceptional efforts have been made in developing therapeutic countermeasures against filoviruses, which recently led to the approval of two EBOV vaccines and a human monoclonal antibody cocktail. However, in spite of the promising results shown by several compound candidates, no small molecule drugs have gained licensing to date (Hansen et al., 2021). This urges for keeping up the pursuit of novel therapeutics on the one hand and for the development of biochemical tools to explore the antiviral target potential of functional domains in filoviral proteins on the other hand (Edwards and Basler, 2019). One of the key aspects that correlates with the high lethality of EBOV and MARV infection is the coupling of viral replication, that proceeds unarrested, together with the potent suppression of the host innate immune response (Olejnik et al., 2017). Among the nine proteins encoded by the filoviral genome, one in particular - the virion protein 35 (VP35) - is involved in both those processes. VP35 is the ortholog of the phosphoprotein (P) of the other viruses in the *Mononegavirales*. It is a modular protein of 340 and 329 amino acids in length in EBOV and MARV, respectively (Figure 1A), whose domain structures have been solved in recent years, thus providing the structural basis to dissect and elucidate its multifunctional nature. In the context of filovirus replication, where VP35 acts as indispensable co-factor for the viral RNA-dependent RNA polymerase (RdRp) large (L) protein, the region responsible for interaction with L is deemed to be located within the central coiled-coil of the oligomerization domain, and VP35 is thought to tether the L polymerase to the ribonucleoprotein (RNP) complex, forming a scaffold for viral

[1]The Max-Planck Institute of Biochemistry, Department of Molecular Structural Biology, Am Klopferspitz 18, 82152 Martinsried, Germany

[2]Istituto Zooprofilattico Sperimentale delle Venezie, Department of Risk Analysis and Public Health Surveillance, Viale dell'Università 10, 35020 Legnaro, Italy

[3]The Max-Planck Institute of Biochemistry, Department of Cellular Biochemistry, Am Klopferspitz 18, 82152 Martinsried, Germany

[4]Lead contact

*Correspondence: zinzula@biochem.mpg.de (L.Z.), baumeist@biochem.mpg.de (W.B.)

https://doi.org/10.1016/j.isci.2022.105354

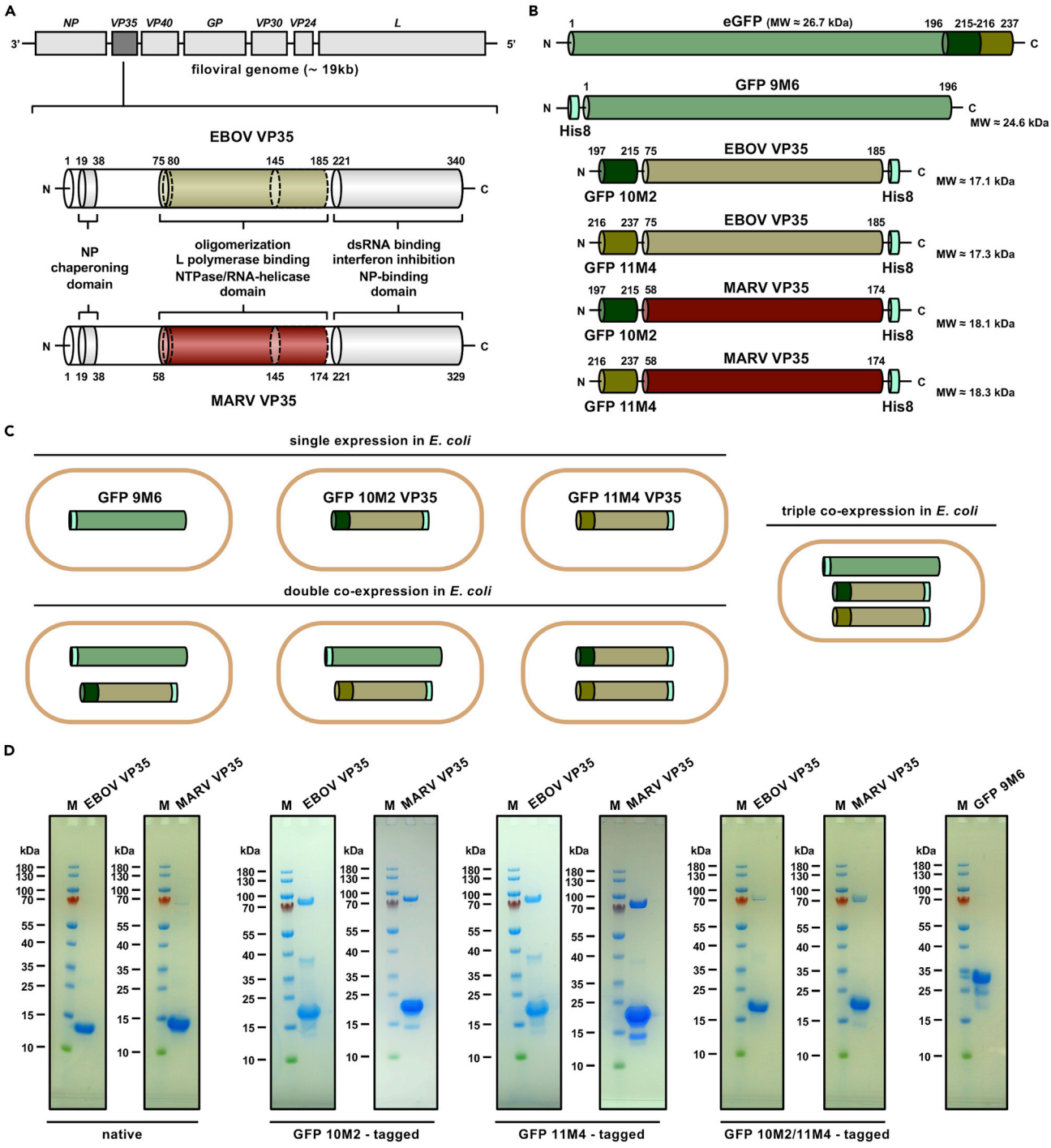

Figure 1. EBOV and MARV VP35 oligomerization domains tripartite split-GFP FC system

(A) Structural organization of EBOV and MARV VP35 proteins; the position of the *VP35* gene in the filoviral genome and the oligomerization domain in the protein of the two filoviral species are highlighted in dark gray and avocado and maroon color, respectively.

(B) Cartoon model illustrating the split of the full-length eGFP into the three components 9M6, 10M2, 11M4 (colored in laurel, dark lime and olive, respectively), and the design of the GFP 10M2-fused EBOV (residues 75–185), MARV (residues 58–174) VP35 oligomerization domains and GFP 9M6 (residues 1–196) recombinant constructs (MW, molecular weight).

(C) Cartoon model illustrating the heterologous expression in *E. coli* cells of recombinant VP35 oligomerization domain fused to split-GFP 10M2 and 11M4 tags, and of GFP 9M6, in various combinations for the single expression, double and triple co-expression of the chimeric proteins.

Figure 1. *Continued*

(D) Blue Coomassie-stained SDS-PAGE analysis of IMAC and SEC purified recombinant EBOV $VP35_{75-185}$ and MARV $VP35_{58-174}$ oligomerization domains (in their native non-tagged and GFP-tagged versions, respectively) and of IMAC and SEC purified recombinant GFP 9M6; oligomeric protein bands resistant to full denaturation by heat, reducing agents and SDS, are visible in most VP35 samples as migrating at ~ 70 kDa; faint bands reminiscent of protein degradation products are visible in most samples as migrating below the monomeric band of the constructs. (M, molecular weight marker).

RNA synthesis (Bruhn et al., 2017; Ramaswamy et al., 2018; Zinzula et al., 2019; Chanthamontri et al., 2019). VP35 also binds to the viral nucleoprotein (NP) via its unstructured N-terminal region, thereby preventing NP protomers from unspecific coating of host and viral RNA, and chaperoning them to the de novo-synthesized viral genome for proper assembly of nascent RNP complexes (Leung et al., 2015; Kirchdoerfer et al., 2015; Zhu et al., 2017; Landeras-Bueno et al., 2019). With respect to innate immunity evasion, VP35 interacts with dsRNA byproducts of viral replication via its C-terminal dsRNA binding/interferon (IFN)-inhibitory domain (RBD/IID). By doing so, VP35 impedes that viral nucleic acids are recognized as pathogen-associated molecular patterns (PAMPs) by cytoplasmic RNA helicases of the retinoic acid-inducible gene I (RIG-I)-like receptors (RLRs) family, ultimately suppressing induction of type I IFN (Leung et al., 2009, 2010a, 2010b; Kimberlin et al., 2010; Bale et al., 2012, 2013; Ramanan et al., 2012; Zinzula et al., 2012). To function as replicative co-factor as well as IFN antagonist, VP35 is required to be in oligomeric form. In fact, alanine mutations of highly conserved hydrophobic residues within the VP35 oligomerization domain (Leu90, Leu93 and Leu107 in EBOV; Leu90 and Leu104 in MARV) disrupt the coiled-coil, thereby abolishing viral replication and potently diminishing VP35 IFN inhibition capability (Reid et al., 2005; Möller et al., 2005). Crystal structures and biophysical in-solution data revealed a trimeric organization of the isolated VP35 oligomerization domain for MARV, trimeric and tetrameric forms for EBOV, and exclusively tetrameric assemblies for all the other ebolaviral species (Bruhn et al., 2017; Zinzula et al., 2019). In both the trimeric and tetrameric states, oligomerization is mediated by a canonical coiled-coil motif consisting of five or four amino acid heptad repeats in EBOV and MARV, respectively. Moreover, residues whose mutation were found to be detrimental to viral replication and immune evasion are located at positions *a* and *d* of the *abcdefg* heptad register, pointing towards the coiled-coil axis to form its inner hydrophobic core (Zinzula et al., 2019). Elucidation of the structural basis for such defective phenotypes has thus reinforced the importance of VP35 function for determinacy of EBOV and MARV virulence and pathogenesis. Furthermore, these mutations have highlighted the potential and attractiveness of the VP35 coiled-coil oligomerization domain as a unique antiviral target. However, no biochemical assay has been established thus far to monitor VP35 oligomerization *in vitro*, and no readout to probe this process for antiviral screening purposes has been available. Previous studies on full-length recombinant constructs showed that no VP35 monomeric species exist in solution (Zinzula et al., 2009; Kimberlin et al., 2010; Bruhn et al., 2017; Ramaswamy et al., 2018). Nonetheless, biophysical characterization of isolated VP35 oligomerization domains revealed that the coiled coil-mediated quaternary structures are highly stable and not subject to a dynamic equilibrium at physiological conditions (Bruhn et al., 2017; Zinzula et al., 2019). Considering that VP35 oligomers presumably form immediately after protein translation, these features limit the investigation on VP35 assemblies to techniques that can detect oligomerization *ex-post facto*. In recent years, a new experimental approach to probe protein-protein interactions has been developed that relies on a tripartite split-green fluorescent protein (GFP) system whose fragments are fused as GFP tags to protein partners. Only as a direct consequence of oligomer formation of the protein partners, the GFP tags can properly orient and mutually interact, then bind to a third GFP fragment that serves as reporter sensor. Hence, upon assembly of the tripartite split-GFP, the full-length GFP protein is reconstituted into a functional fluorophore, which is termed fluorescence complementation (FC) (Cabantous et al., 2013). The technique was proven to efficiently detect protein-protein interactions in mammalian and *E. coli* cells, with very low fluorescence background and lack of false-positives that because of the spontaneous self-association of GFP-tags even in the absence of complex formation between the tagged partners, occasionally arise in conventional bimolecular FC (Koraïchi et al., 2018). The central α-helical region of the VP35 oligomerization domain is the one bearing the coiled-coil motif that self-associates in parallel orientation to build homo-trimeric or homo-tetrameric assemblies (Bruhn et al., 2017; Zinzula et al., 2019). The vicinity between α-helices in both oligomeric forms, the intrinsic high stability of their coiled-coil and the high degree of solubility of this domain compared to the full-length protein, render the VP35 oligomerization domain particularly suitable for the placement of small non-perturbing fusion tags at its boundaries. Therefore, we exploited the properties of the tripartite split-GFP system by engineering the EBOV and MARV VP35 oligomerization domains, which we used to establish a novel biochemical assay that makes VP35 oligomerization accessible to inhibitor screening.

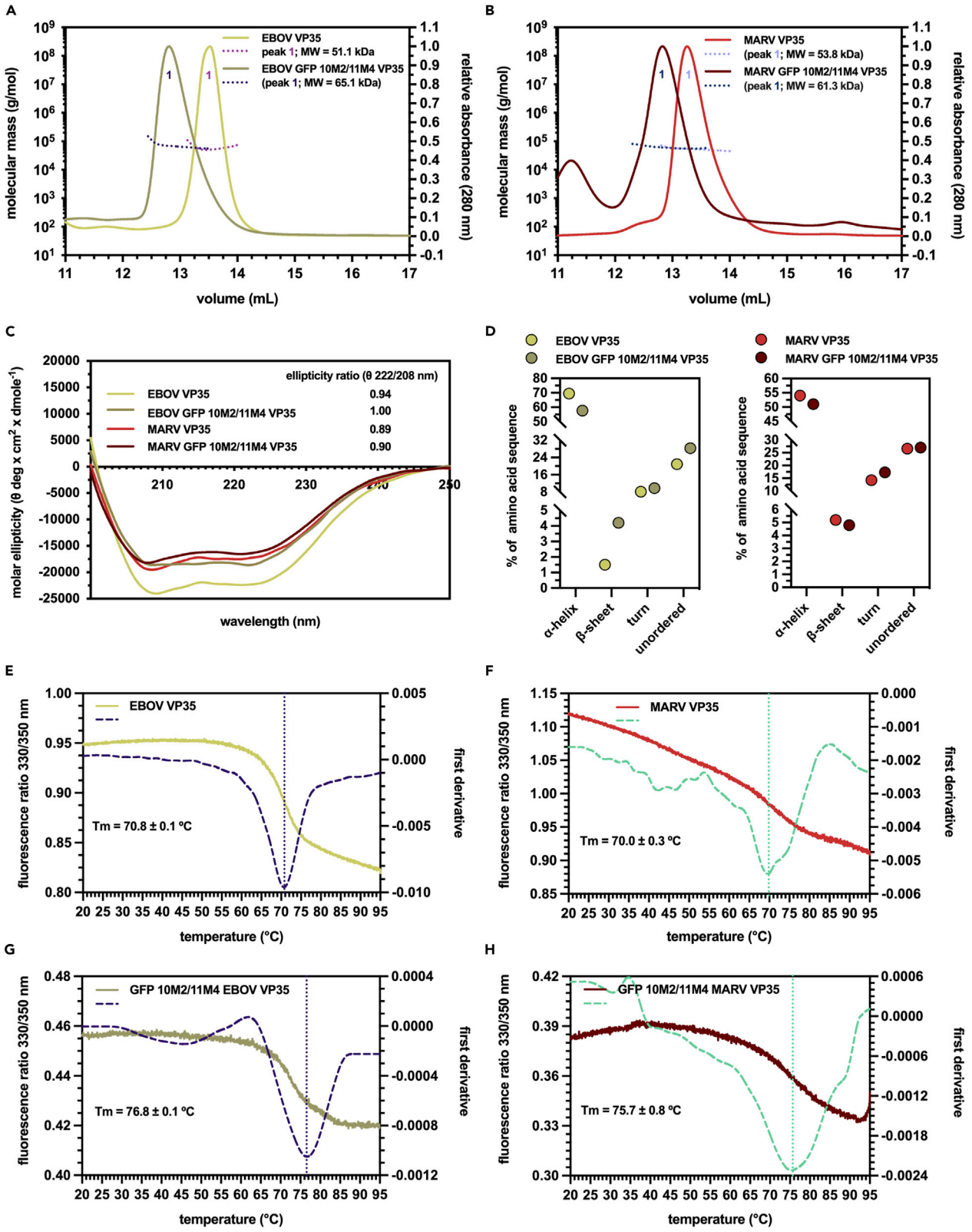
A
molecular mass (g/mol)
relative absorbance (280 nm)
volume (mL)
EBOV VP35
peak 1; MW = 51.1 kDa
EBOV GFP 10M2/11M4 VP35
(peak 1; MW = 65.1 kDa)
B
molecular mass (g/mol)
relative absorbance (280 nm)
volume (mL)
MARV VP35
(peak 1; MW = 53.8 kDa)
MARV GFP 10M2/11M4 VP35
(peak 1; MW = 61.3 kDa)
C
molar ellipticity (θ deg x cm² x dmole⁻¹)
wavelength (nm)
ellipticity ratio (θ 222/208 nm)
EBOV VP35 0.94
EBOV GFP 10M2/11M4 VP35 1.00
MARV VP35 0.89
MARV GFP 10M2/11M4 VP35 0.90
D
EBOV VP35
EBOV GFP 10M2/11M4 VP35
MARV VP35
MARV GFP 10M2/11M4 VP35
% of amino acid sequence
α-helix
β-sheet
turn
unordered
E
fluorescence ratio 330/350 nm
first derivative
temperature (°C)
EBOV VP35
Tm = 70.8 ± 0.1 °C
F
fluorescence ratio 330/350 nm
first derivative
temperature (°C)
MARV VP35
Tm = 70.0 ± 0.3 °C
G
fluorescence ratio 330/350 nm
first derivative
temperature (°C)
GFP 10M2/11M4 EBOV VP35
Tm = 76.8 ± 0.1 °C
H
fluorescence ratio 330/350 nm
first derivative
temperature (°C)
GFP 10M2/11M4 MARV VP35
Tm = 75.7 ± 0.8 °C

Figure 2. Biophysical characterization of co-expressed and purified GFP-tagged EBOV and MARV VP35 oligomerization domains

(A) SEC-MALS analysis showing the quaternary structure in-solution profile of EBOV $VP35_{75-185}$ and GFP 10M2/11M4 EBOV $VP35_{75-185}$. (B) SEC-MALS analysis showing the quaternary structure in-solution profile of MARV $VP35_{58-174}$ and GFP 10M2/11M4 MARV $VP35_{58-174}$. (C) Far-UV CD spectra of EBOV $VP35_{75-185}$, GFP 10M2/11M4 EBOV $VP35_{75-185}$, MARV $VP35_{58-174}$and GFP 10M2/11M4 MARV $VP35_{58-174}$. (D) Far-UV CD spectra deconvolution and secondary structure content analysis of EBOV $VP35_{75-185}$ and GFP 10M2/11M4 EBOV $VP35_{75-185}$ (left panel), MARV $VP35_{58-174}$ and GFP 10M2/11M4 MARV $VP35_{58-174}$ (right panel). (E) Nano-DSF analysis showing the conformational profile and thermal stability of native non-tagged EBOV $VP35_{75-185}$ and (F)MARV $VP35_{58-174}$. (G) Nano-DSF analysis showing the conformational profile and thermal stability of GFP-tagged GFP 10M2/11M4 EBOV $VP35_{75-185}$ and (H) GFP 10M2/11M4 MARV $VP35_{58-174}$.

RESULTS AND DISCUSSION

Design of a tripartite split-GFP FC system to probe EBOV and MARV VP35 oligomerization

Recombinant EBOV (residues 75–185) and MARV (residues 58–174) VP35 constructs (Figure 1A) were designed for bacterial expression, each N-terminally fused with either GFP β-strand 10M2 (residues 197–215) or GFP β-strand 11M4 (residues 216–237) tags of the enhanced GFP (eGFP, residues 1–237) (Figures 1B, 1C, S1, and S2). These constructs are longer versions of the VP35 oligomerization domain as compared to previous ones (Bruhn et al., 2017; Zinzula et al., 2019), containing an amino acid tract upstream to the canonical coiled coil and downstream its adjacent highly conserved amphipathic chain, the latter of which was recently found capable of nucleoside triphosphatase (NTPase)/helicase activity (Shu et al., 2019). Also, a recombinant GFP truncation derived from the previously described GFP 1–9 OPT fragment (residues 1–193) (Cabantous et al., 2013) and here named as GFP 9M6 (residues 1–196), was designed to function as detector component in the tripartite system (Figures 1B and S1). Recombinant proteins bearing an N-terminal (for GFP 9M6) or C-terminal (for GFP 10M2-and GFP 11M4-fused VP35) octahistidine (His8) tag were all expressed in *E. coli*, singly or co-expressed in all the combinations of two and three components (Figures 1B, 1C, and S2), then purified by immobilized metal-ion affinity chromatography (IMAC) and by size exclusion chromatography (SEC) followed by sodium dodecyl sulphate-polyacrylamide gel electrophoresis (SDS-PAGE) analysis (Figure 1D). Fractions corresponding to the main SEC peak of co-expressed GFP 10M2/11M4 VP35 oligomerization domains were pooled, then subjected to comparative biophysical characterization with respect to the native, non GFP-tagged VP35 constructs added of a hexahistidine (His6) tag at their C-termini, which were taken as controls (Figure S3). Analysis of the in solution oligomeric state by SEC coupled to multi-angle light scattering (SEC-MALS) showed that GFP 10M2/11M4 EBOV VP35 and non GFP-tagged EBOV VP35 oligomerization domains eluted each as major peak with average molecular weight (MW) of about 65.1 and 51.1 kDa, respectively (Figure 2A). Similarly, GFP 10M2/11M4 MARV VP35 and non-GFP tagged MARV VP35 oligomerization domains eluted as major peak with average MW of ∼61.3 and ∼53.8 kDa, respectively (Figure 2B). Considering the predicted monomeric size of ∼17.2 kDa (GFP 10M2/11M4-tagged, average) and ∼13.3 kDa (non GFP-tagged) for the EBOV construct, and of ∼18.1 kDa (GFP 10M2/11M4-tagged, average) and ∼14.3 kDa (non GFP-tagged) for the MARV one, these values correspond to 3.7–3.8 and 3.4–3.7-folds the EBOV and MARV VP35 oligomerization domain monomer, respectively. Hence, they are consistent with a mixed population of homo-trimers and homo-tetramers in solution, in agreement to what previously observed for filoviral VP35 oligomers (Zinzula et al., 2009, 2019; Kimberlin et al., 2010; Bruhn et al., 2017; Ramaswamy et al., 2018). Far-UV circular dichroism (CD) spectroscopy showed that, likewise their non GFP-tagged counterparts, GFP 10M2/11M4 EBOV and MARV VP35 oligomerization domains display an overall α-helical folding profile (Figures 2C and 2D). Moreover, the θ 222/208 nm ellipticity ratio values of both non-tagged and GFP-tagged constructs slightly deviate from those typical of coiled-coils (θ 222/208 nm ≥ 1) previously observed for shorter versions of the VP35 oligomerization domain (Zinzula et al., 2019), in agreement with bioinformatic secondary structure prediction for the added residues, located upstream the coiled-coil and downstream the C-terminal amphipathic chain, of being folded as short α-helices interspersed with flexible regions (Figure S3). Consistent with this notion, miniaturized differential scanning fluorimetry (Nano-DSF) showed that such versions of the EBOV and MARV VP35 oligomerization domain have melting temperature (Tm) values of ∼71 and 70°C, respectively (Figures 2E and 2F), which albeit indicative of stable proteins, are lower than those previously reported for VP35 oligomerization domain constructs narrowed to the sole coiled-coil and its C-terminal amphipathic chain (Bruhn et al., 2017; Zinzula et al., 2019). Nevertheless, inclusion of the 10M2 and 11M4 β-strands resulted in an increase in thermal stability, with melting temperature (Tm) values of ∼77 and ∼76°C for the co-expressed GFP 10M2/11M4 EBOV and MARV VP35 oligomerization domains, respectively (Figures 2G and 2H). Overall, these results demonstrate that addition of the two GFP tags does not significantly change the properties of EBOV and MARV VP35 oligomerization domains in terms of oligomeric state, α-helical folding and stability, thus allowing the use of such constructs as models to study the protein-protein interactions underlying the VP35 oligomerization process.

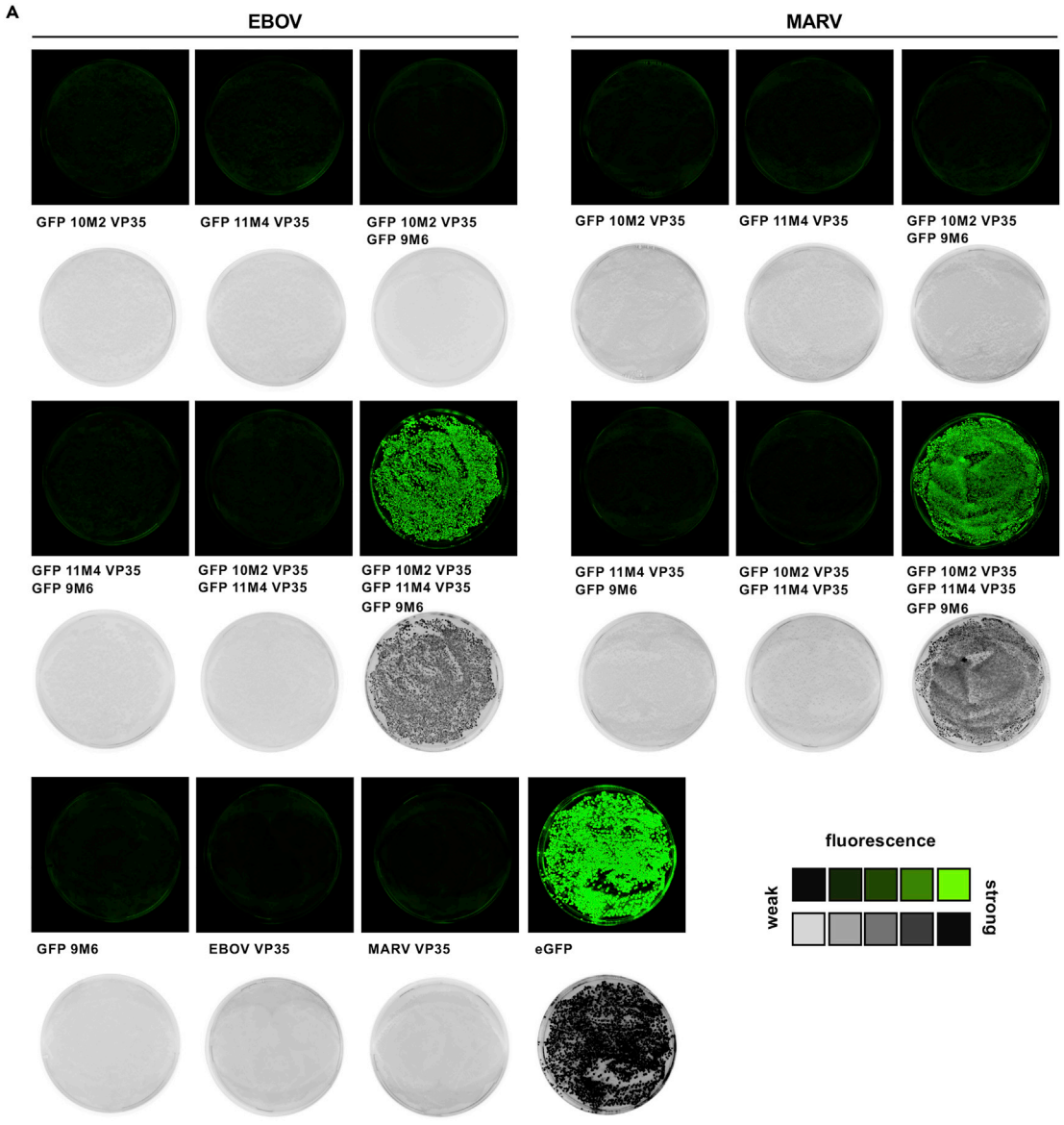
A
EBOV
MARV
GFP 10M2 VP35
GFP 11M4 VP35
GFP 10M2 VP35
GFP 9M6
GFP 10M2 VP35
GFP 11M4 VP35
GFP 10M2 VP35
GFP 9M6
GFP 11M4 VP35
GFP 9M6
GFP 10M2 VP35
GFP 11M4 VP35
GFP 11M4 VP35
GFP 9M6
GFP 10M2 VP35
GFP 11M4 VP35
GFP 10M2 VP35
GFP 11M4 VP35
GFP 9M6
GFP 9M6
EBOV VP35
MARV VP35
eGFP
fluorescence
weak
strong
B
EBOV
MARV
fluorescence counts
8×10^4
7×10^4
6×10^4
5×10^4
4×10^4
3×10^4
3500
3000
2500
2000
1500
1000
500
0
eGFP
FC cis VP35
GFP 9M6
GFP 10M2/11M4 VP35
GFP 10M2 VP35
GFP 11M4 VP35
VP35
FC trans VP35

Figure 3. Split-GFP FC screening of EBOV and MARV VP35 oligomerization *in vivo* and *in vitro*

(A) *In vivo* screening of fluorescence in *E. coli* colonies on agar plates (EBOV, left panel; MARV, right panel): FC results from the co-expression of GFP 102/11M4 EBOV $VP35_{75\text{-}185}$ or GFP 102/11M4 MARV $VP35_{58\text{-}174}$ with GFP 9M6, whereas co-expression of GFP 10M2 EBOV $VP35_{75\text{-}185}$ or MARV $VP35_{58\text{-}174}$, and GFP 11M4 EBOV $VP35_{75\text{-}185}$ or MARV $VP35_{58\text{-}174}$ with GFP 9M6 leads to close-to-background fluorescence only. Singly expressed full-length eGFP, GFP 9M6, GFP-tagged and non-tagged EBOV $VP35_{75\text{-}185}$ and MARV $VP35_{58\text{-}174}$ constructs are shown as controls.

(B) *In vitro* screening of fluorescence in eGFP reconstitution reactions (EBOV, left panel; MARV, right panel): FC resulting from the oligomerization of co-expressed and purified GFP 10M2/11M4 EBOV $VP35_{75\text{-}185}$ and MARV $VP35_{58\text{-}174}$ mixed with purified GFP 9M6 (FC_{cis} VP35), produces a fluorescence signal comparable to that of full-length eGFP. FC resulting from the oligomerization of singly-expressed and purified GFP 10M2 EBOV $VP35_{75\text{-}185}$ or MARV $VP35_{58\text{-}174}$, and GFP 11M4 EBOV $VP35_{75\text{-}185}$ or MARV $VP35_{58\text{-}174}$, mixed after purification with each other and with purified GFP 9M6 (FC_{trans} VP35) leads to a fluorescence signal that is about 20-fold lower. Singly expressed and purified full-length eGFP, GFP 9M6, GFP-tagged and non-tagged EBOV $VP35_{75\text{-}185}$ and MARV $VP35_{58\text{-}174}$ constructs are shown as controls.

Importantly, considering the plasticity displayed by filoviral VP35 coiled coils, which were previously shown to assemble into different, however nearly-isoenergetic oligomeric states (Ramaswamy et al., 2018; Zinzula et al., 2019; Di Palma et al., 2019), it is worth noting that the designed tripartite FC system is fully compatible with the formation of both VP35 homo-trimers and homo-tetramers. In fact, assuming no variation in the expression rate between the two GFP-tagged VP35 monomers (i.e., fused to GFP 10M2 or GFP 11M4), the different assortments of the two tags for a given VP35 oligomer are in principle equiprobable and, regardless whether the resulting oligomer is a homo-trimer or a homo-tetramer, the presence of two GFP tags represents the minimum requirement for the FC signal to occur (Figure S4A).

Functional GFP is reconstituted upon EBOV and MARV VP35 oligomerization *in vivo* and *in vitro*

Next, we wanted to evaluate whether the reconstitution of the GFP ternary complex, and therefore the FC, would occur *in vivo* and could be monitored through the rapid screening of fluorescent *E. coli* cell colonies. To this aim, agar plates seeded with triple transformants - concomitantly expressing GFP 9M6, GFP 10M2 VP35 and GFP 11M4 VP35 were compared to those with double transformants in various combinations and with single transformants. Only the co-expression of all components of the tripartite system – namely the VP35 oligomerization domains fused to the GFP 10M2 and 11M4 tags and the GFP 9M6 reporter – led to the growth of bright and fluorescent bacterial colonies, whereas negligible fluorescence comparable to the background was observed when one or more of the components were missing (Figure 3A). In parallel, the *in vitro* reconstitution of the GFP ternary complex by mixing purified EBOV and MARV GFP 10M2/11M4 VP35 with GFP 9M6 was assessed. To this aim, reactions were set up in 50–100 μL volume replicates on 96- or 384-well plates under close-to-physiological conditions (25 mM Tris pH 7.4, 100 mM NaCl), incubated for 1 h to allow the tethering of GFP 10M2/11M4 to GFP 9M6, followed by detection of the fluorescent signal. For both EBOV and MARV VP35, only the oligomers bearing both types of GFP tags, formed upon co-expression of GFP 10M2-and GFP 11M4-fused VP35, could reconstitute a full-length functional GFP when mixed after purification with an excess of the truncated GFP 9M6 reporter (Figure 3B). Moreover, complexes containing all three components showed fluorescence similar to intact eGFP (Figure 3B, bars FC_{cis} VP35 WT). By contrast, as in the agar-plate screening, controls missing one or more components exhibited very little or no fluorescence. Of note, the ability to reconstitute a functional chromophore could not be fully restored when VP35 bearing the missing GFP-tag was provided in *trans* by adding the corresponding purified protein to the reaction (Figure 3B, bars FC_{trans} VP35 WT). On the one hand, this is a confirmation of the previous observation that once formed VP35 oligomers do not undergo dynamic dissociation and re-assembly (Zinzula et al., 2019). On the other hand, this rules out the possibility that two complementary GFP tags, remained uncoupled in their respective VP35 homo-trimers, may interact with GFP 9M6 and reconstitute a "bridged" full-length GFP, thereby leading to false positive read-outs that do not represent VP35 oligomerization-dependent FC events. Instead, results demonstrate that FC of the tripartite split-GFP, *in vivo* as well as *in vitro*, directly correlates with the preemptive formation of EBOV and MARV VP35 oligomers bearing an assortment of the two different GFP tags 10M2 and 11M4.

Optimal biochemical parameters to monitor EBOV and MARV VP35 oligomerization by GFP FC

Probing the EBOV and MARV VP35 oligomerization in a quantitative and reproducible manner required our assay to be robust, sensitive and also fast to be suitable for screening. Moreover, one peculiarity of adopting the tripartite split-GFP system to study this process is that, in contrast to other methods, protein-protein complex formation can be detected in this case only in retrospect. In addition, the ratio between the two types of tags GFP 10M2 and GFP 11M4 in a given VP35 oligomer is not tunable, because

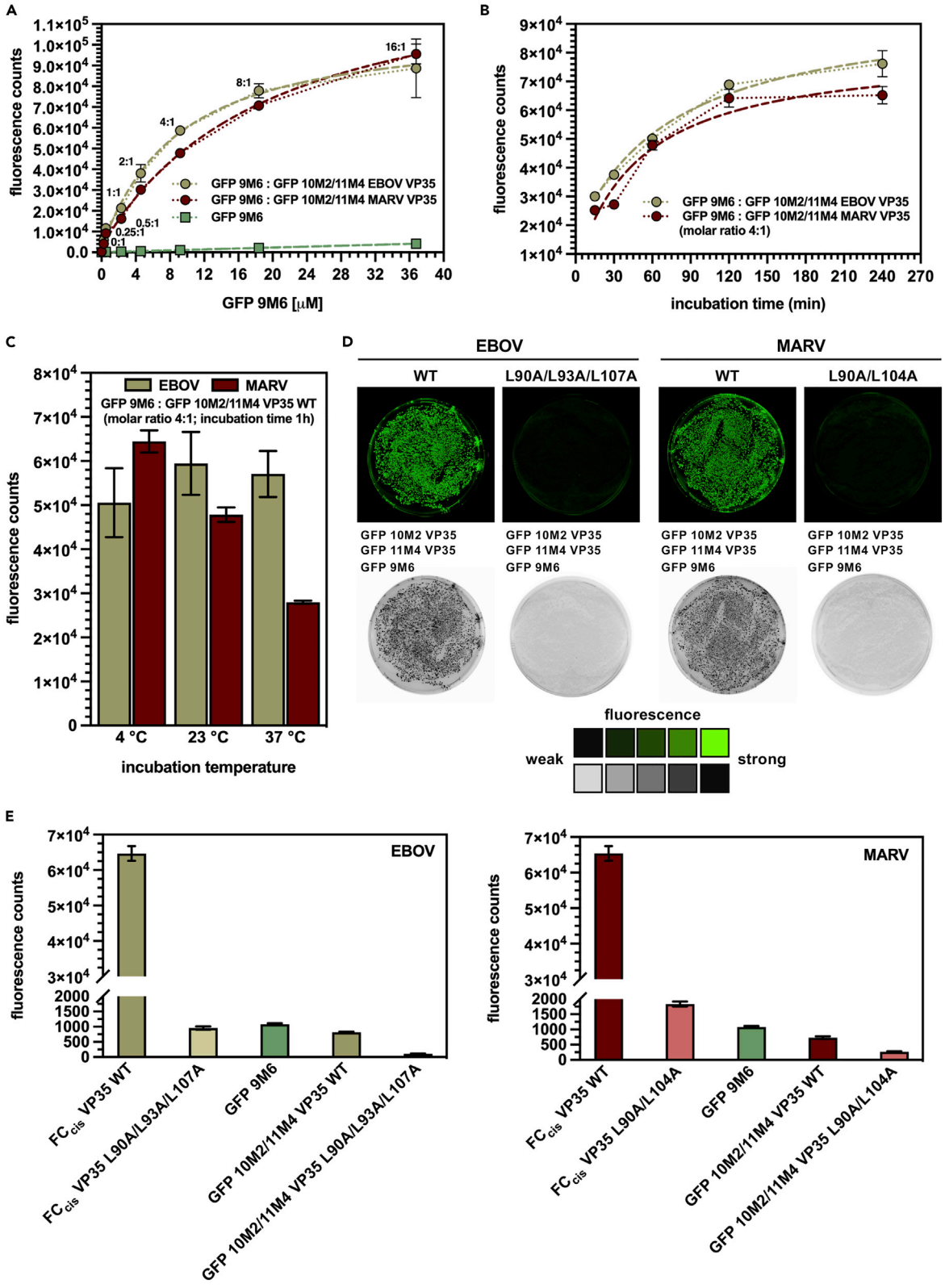
A
fluorescence counts
GFP 9M6 [μM]
GFP 9M6 : GFP 10M2/11M4 EBOV VP35
GFP 9M6 : GFP 10M2/11M4 MARV VP35
GFP 9M6
1:1
2:1
4:1
8:1
16:1
0.5:1
0.25:1
0:1
B
fluorescence counts
incubation time (min)
GFP 9M6 : GFP 10M2/11M4 EBOV VP35
GFP 9M6 : GFP 10M2/11M4 MARV VP35
(molar ratio 4:1)
C
EBOV
MARV
GFP 9M6 : GFP 10M2/11M4 VP35 WT
(molar ratio 4:1; incubation time 1h)
fluorescence counts
4 °C
23 °C
37 °C
incubation temperature
D
EBOV
MARV
WT
L90A/L93A/L107A
WT
L90A/L104A
GFP 10M2 VP35
GFP 11M4 VP35
GFP 9M6
fluorescence
weak
strong
E
EBOV
MARV
fluorescence counts
FC cis VP35 WT
FC cis VP35 L90A/L93A/L107A
GFP 9M6
GFP 10M2/11M4 VP35 WT
GFP 10M2/11M4 VP35 L90A/L93A/L107A
FC cis VP35 L90A/L104A
GFP 10M2/11M4 VP35 L90A/L104A

Figure 4. Optimization of split-GFP FC biochemical parameters and validation by oligomerization-defective EBOV and MARV VP35 mutants

(A) Characterization of the optimal molar ratio between *i)* co-expressed and purified GFP 10M2/11M4 EBOV $VP35_{75-185}$ or GFP 10M2/11M4 MARV $VP35_{58-174}$ and *ii)* purified GFP 9M6 in FC *in vitro* reactions.

(B) Dependence of *in vitro* FC on the incubation time between *i)* co-expressed and purified GFP 10M2/11M4 EBOV $VP35_{75-185}$ or GFP 10M2/11M4 MARV $VP35_{58-174}$ and *ii)* purified GFP 9M6.

(C) Dependence on the incubation temperature of the *in vitro* FC between *i)* co-expressed and purified GFP 10M2/11M4 EBOV $VP35_{75-185}$ or GFP 10M2/11M4 MARV $VP35_{58-174}$ and *ii)* purified GFP 9M6.

(D) *In vivo* screening of fluorescence in *E. coli* colonies on agar plates (EBOV, left panel; MARV right panel) resulting from the aberrant oligomerization of co-expressed GFP 10M2/11M4 EBOV $VP35_{75-185}$ L90A/L93A/L107A or GFP 10M2/11M4 MARV $VP35_{58-174}$ L90A/L104A, and consequent loss of, or reduced FC, with co-expressed GFP 9M6; WT constructs are shown as positive controls.

(E) *In vitro* screening of fluorescence in eGFP reconstitution reactions (EBOV, left panel; MARV, right panel) resulting from the aberrant oligomerization of co-expressed and purified EBOV $VP35_{75-185}$ L90A/L93A/L107A or GFP 10M2/11M4 MARV $VP35_{58-174}$ L90A/L104A, and consequent loss of, or reduced FC, when mixed to purified GFP 9M6. Singly expressed and purified GFP 9M6, Co-expressed and purified GFP-tagged EBOV $VP35_{75-185}$ WT and GFP-tagged MARV $VP35_{58-174}$ WT are shown as controls.

it derives from stochastic assortment. Hence, as long as that the presence of both 10M2 and 11M4 tags is ensured by co-expression of the respective GFP-tagged VP35 species, the amount of GFP 9M6 detector represents the only limiting reagent for FC to occur. We therefore aimed to define to what minimum excess, for how long and in which optimal biochemical conditions the detector component should be added to saturate the system for the best signal-to-noise ratio. We characterized the optimal assay parameters in terms of molar ratio between the GFP 9M6 detector and the GFP 10M2/11M4-fused VP35 oligomer, as well as in terms of incubation time and temperature. A titration experiment was conducted against a fixed molar amount ($\approx$2.3 μM) of the co-expressed GFP 10M2/11M4 EBOV (or MARV) VP35 oligomerization domains, by varying the GFP 9M6 concentration by two-fold serial dilutions between 36.8 and 0.575 μM. In both EBOV and MARV samples, fluorescence steeply increased with increasing GFP 9M6 concentration up to a 4:1 M ratio between GFP 9M6 and GFP 10M2/11M4-tagged VP35, after which the fluorescence yield began to level off, (Figure 4A). Conversely, although the signal provided by the intrinsic fluorescence of the GFP 9M6 negative control increased linearly and proportionally to its molar amount, intensity remained close to background level even at the highest concentration tested (Figure 4A). Fluorescence was also measured at a 4:1 ratio over an incubation period of 15–240 min. Signal intensity steeply increased up to 60 min and gradually leveled off toward 240 min (Figure 4B). Furthermore, the fluorescence at three different incubation temperatures (4, 23 and 37°C) was recorded, showing no significant variation for the EBOV VP35 construct, whereas a decrease in signal intensity with increasing temperature was observed for MARV VP35 (Figure 4C). On the basis of these results, a 4:1 M ratio between GFP 9M6 and GFP 10M2/11M4-tagged VP35 oligomerization domains, 60 min incubation time and 23°C incubation temperature were chosen to conduct all subsequent experiments.

Defective assembly of EBOV and MARV VP35 coiled coil correlates with loss of GFP FC

Next, we wanted to assess the suitability of the assay to study oligomerization-related VP35 gain- or loss-of-function arising from mutagenesis. To this aim, we co-expressed and purified the GFP 10M2/11M4-tagged EBOV VP35 L90A/L93A/L107A triple and MARV VP35 L90A/L104A double mutants (Figure S5A), which were previously found to be oligomerization-defective and reported to impair VP35 suppression of the host interferon response and virus replication, respectively (Reid et al., 2005; Möller et al., 2005). In agreement with previous results obtained for non GFP-tagged constructs bearing these mutations (Zinzula et al., 2019), biophysical characterization of GFP 10M2/11M4 EBOV VP35 L90A/L93A/L107A and GFP 10M2/11M4 MARV VP35 L90A/L104A oligomerization domains supported full disruption of the coiled-coil folding. In fact, SEC-MALS showed that both EBOV and MARV GFP-tagged VP35 mutants tend to multimerize into oligomeric forms of high MW (Figure S5B). Moreover, far-UV CD spectra profiles resembled those of unstructured proteins (Figures S5C and S5D), suggesting that such multimers are the result of an aberrant assembly that does not rely on coiled-coil knobs-into-holes packing. In addition, Nano-DSF analysis of GFP 10M2/11M4-tagged EBOV VP35 L90A/L93A/L107A and MARV VP35 L90A/L104A mutants showed lower Tm values with respect to WT and two inflection points (EBOV, ~ 49°C and ~64°C versus ~77°C; MARV, 40 and ~60°C versus ~76°C), indicating that both these mutants are inherently less stable (Figures S5E and S5F). Furthermore, the *in vivo* FC screening agreed with biophysical experiments, as colonies of triple transformant *E. coli* cells expressing all three components of the split-GFP tripartite system displayed low fluorescence close to background level (Figure 4D). Also, in the *in vitro* assay, both co-expressed and purified GFP 10M2/11M4 EBOV VP35 L90A/L93A/L107A and GFP 10M2/11M4 MARV VP35 L90A/L104A oligomers failed to reconstitute a full-length GFP when incubated with the GFP 9M6 reporter, as shown by

decreases in the fluorescence signal by approximately 98 and 97%, respectively, as compared to WT (Figure 4E). Taken together, these results demonstrate that fluorescence of the complemented tripartite split-GFP depends on the nature of the side chains that interact in the EBOV and MARV VP35 coiled-coil, and that disruption or destabilization of the VP35 quaternary structure directly correlates with loss or reduction of GFP fluorescence (Figure S4B).

Validation of tripartite split-GFP FC system for screening antiviral candidates perturbing EBOV and MARV VP35 coiled coil assembly

Finding a small-molecule compound is able to entirely disrupt the α-helix interactions within a coiled-coil appears an arduous challenge. In fact, the hydrophobic interactions tightening the knobs-into-holes packing system, as well as the electrostatic ones clamping the α-helices outer shell through inter- and intra-chain salt bridges, are highly stable and thermodynamically favored (Lupas and Bassler, 2017). Nonetheless, small molecule inhibitors of respiratory syncytial virus (Roymans et al., 2010), human immunodeficiency virus (McGee et al., 2017) and Middle East respiratory syndrome coronavirus (Kandeel et al., 2020) fusion proteins are all representative examples of the fact that even subtle perturbations of the coiled-coil helical properties and conformation arising from the binding of a ligand to its accessible pockets may have dramatic consequences on the domain function. With this in mind, we sought to evaluate how the local destabilization of the coiled-coil register – be it the result of a disruptive mutation or the interaction with a ligand – would affect the conformation at the distal portions of the oligomerization domain where the two GFP-tags are attached. To this aim, we first performed explorative molecular dynamics (MD) simulations on the solved crystallographic structures of the EBOV and MARV VP35 trimeric coiled-coils and on the modeled structure of the EBOV tetrameric one, comparing the WT constructs to their oligomerization-defective mutant counterparts. As shown by the analysis of MD trajectories (Figures S6 and S7), Leu to Ala substitutions at *a* and *d* positions of the coiled-coil hydrophobic core introduce irregularities into the knob-into-holes pairing system, leading the coiled-coil superhelix to partially unwind and the α-helices to slightly depart from each other (Figures S8–S10). This rationalizes the failure of VP35 oligomers to keep their α-helices in proper conformation, which is essential for GFP 10M2 and 11M4 tags to get in contact with the GFP 9M6 reporter and undergo FC. We then benchmarked the FC assay by using for pilot screening a set of small molecules (N = 8) from an in-house library of chemical compounds (Figure S11A), and found that the two compounds Myricetin (Figure 5A) and 4,5,6,7-Tetrabromobenzotriazole (TBBT) (Figure 5B) inhibited the VP35 oligomerization-mediated split-GFP FC (Figures S12A and S12B). Myricetin prevented the coiled-coil of EBOV and MARV VP35 oligomerization domains from assuming their correct conformation, showing IC_{50} values of 64.4 and 25.5 μM, respectively (Figures 5C and 5E). Similarly, the inhibitory effect exerted by TBBT resulted in IC_{50} values of 32.5 and 9.8 μM, respectively (Figures 5D and 5F). Calculation of the assay Z′-factor yielded a value of 0.71, which is indicative of assay robustness (Zhang et al., 1999). Moreover, both Myricetin and TBBT neither displayed intrinsic fluorescence, nor diminished that of a full-length eGFP (Figure S11B). Instead, Nano-DSF showed that both compounds specifically interact with EBOV and MARV VP35 oligomerization domains. In fact, when tested on the VP35 constructs devoid of the GFP 10M2 and 11M4 tags at concentrations corresponding to the split-GFP FC IC_{50} value or higher in excess (e.g. 100 μM), Myricetin and TBBT were both able to induce a shift in the Tm of the native (non GFP-tagged) EBOV and MARV VP35 oligomerization domains (Figure S12C). In particular, the Tm value of both EBOV and MARV VP35 oligomerization domains was higher in the presence of Myricetin (EBOV: 70.8, 73.2 and 73.5°C for 0, 64.5 and 100 μM Myricetin, respectively; MARV: 70.0, 74.3 and 75.4°C for 0, 25.5 and 100 μM Myricetin, respectively) (Figures 2E, 2F, S13A, and S13B). Of interest, Myricetin was previously shown to intercalate into the hydrophobic core of the coiled-coil SNARE complex (Yang et al., 2010), and to increase the Tm value of rhodopsin, thereby enhancing its thermal stability upon rigidification of its α-helical bundle (Ortega et al., 2019). Also, Myricetin was reported to interact with EBOV VP35 RBD/IID, while inhibiting its dsRNA binding and IFN antagonism functions (Daino et al., 2018; Corona et al., 2022). Within this picture, from the results here shown it is tempting to speculate that Myricetin may act on VP35 by concomitantly targeting two different domains, thereby having a synergistic inhibitory effect on its functionalities. Conversely, both EBOV and MARV VP35 oligomerization domains displayed lower Tm values in the presence of TBBT (EBOV: 70.8, 67.4 and 66.9°C for 0, 32.5 and 100 μM TBBT, respectively; MARV: 70.0, 64.0 and 59.8°C for 0, 10 and 100 μM TBBT, respectively) (Figures 2E, 2F, S13C, and S13D). Noteworthy, TBBT and its derivatives were previously reported to inhibit the activity of hepatitis C virus, West Nile virus and Japanese encephalitis virus NTPase/helicases (Borowski et al., 2003; Bretner et al., 2005). Of interest, such enzymatic function has been ascribed to the C-terminal amphipathic region downstream of the VP35 coiled coil (Shu et al., 2019), tempting to speculate that binding of TBBT to the VP35

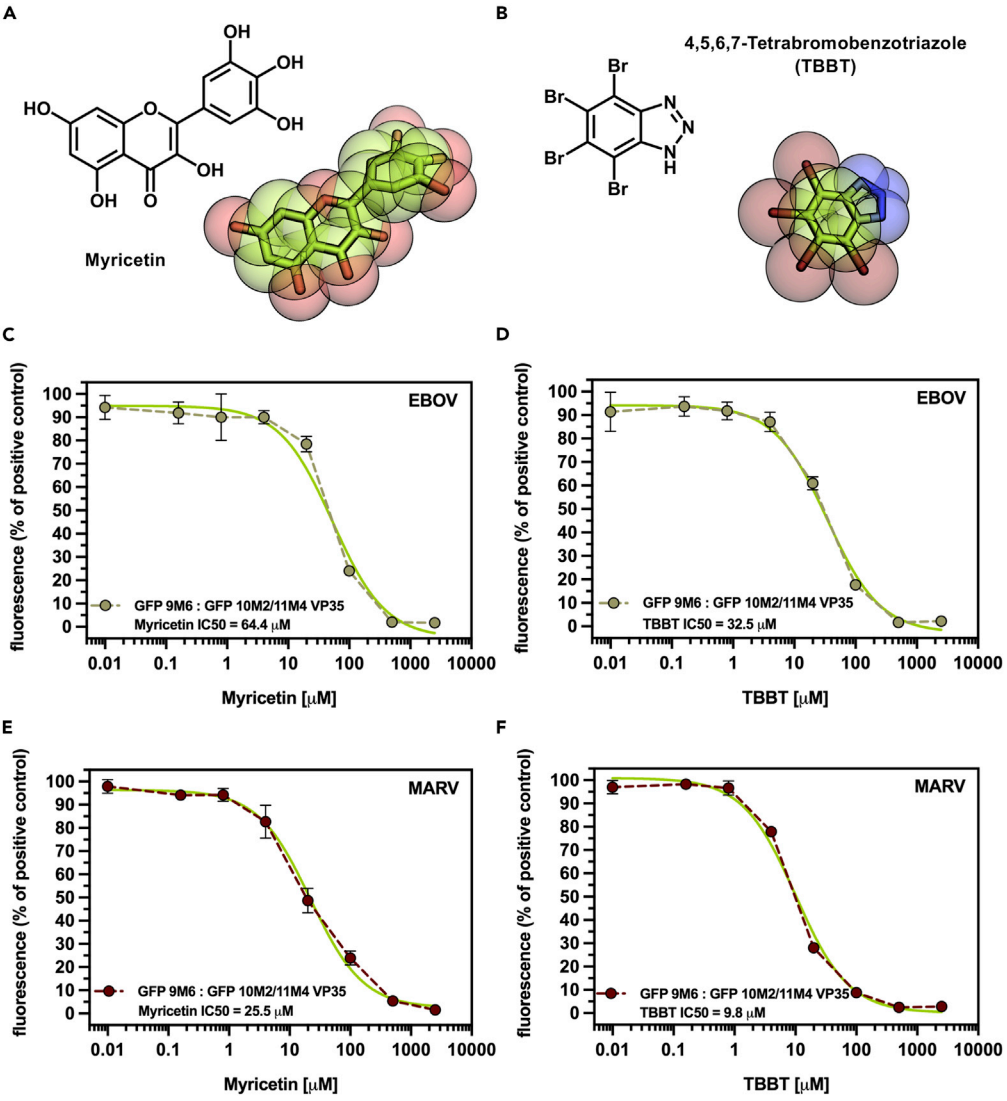

Figure 5. Validation of Split-GFP FC system for antiviral screening of compounds interfering with EBOV and MARV VP35 coiled-coil assembly-mediated oligomerization

(A) Chemical structure of Myricetin and (B) TBBT.

(C) Dose-response inhibition curve by Myricetin on the FC of split-GFP driven by oligomerization of GFP 10M2/11M4 EBOV $VP35_{75\text{-}185}$.

(D) Dose-response inhibition curve by TBBT on the FC of split-GFP FC driven by oligomerization of GFP 10M2/11M4 EBOV $VP35_{75\text{-}185}$.

(E) Dose-response inhibition curve by Myricetin on the FC of split-GFP driven by oligomerization of GFP 10M2/11M4 MARV $VP35_{58\text{-}174}$.

(F) Dose-response inhibition curve by TBBT on the FC of split-GFP FC driven by oligomerization of GFP 10M2/11M4 MARV $VP35_{58\text{-}174}$.

oligomerization domain may also affect its NTPase/helicase activity and suggesting further studies on this direction.

Prediction of Myricetin and TBBT mode of binding on EBOV and MARV VP35 coiled coil reveals druggable pockets

To gain insight on the mode of action of the two ligands, we performed blind molecular docking experiments. For the trimeric and tetrameric structures of the EBOV VP35 oligomerization domain, the best binding poses showed that Myricetin and TBBT insert into a pocket created by the intertwining of the α-helical

chains across the second and the fourth heptad repeats of the coiled-coil canonical register, a region that overlaps with the residues at *d* positions Leu93 and Leu107 that are essential for proper knobs-into-holes pairing (Figures 6A, 7A, and S14). Similarly, for the trimeric structure of the MARV VP35 oligomerization domain, the best binding poses showed that both Myricetin and TBBT insert into a pocket that overlaps (or is adjacent to) the fifth (non-canonical) heptad repeat of the coiled-coil canonical register, whose position *a* corresponds to that of Leu104, also critical for coiled-coil proper assembly (Figures 6B and 7B). Overall, results from molecular docking suggest that the inhibitory effect of Myricetin and TBBT toward FC of the split-GFP recapitulates, at least in part, the one resulting from the introduction of oligomerization-defective mutations such as L90A/L93A/L107A in EBOV VP35 and L90A/L104A in MARV VP35. By interposing between the coiled-coil helices, both compounds likely determine conformational modifications upstream and downstream of their point of insertion that somehow make the GFP 10M2 and 11M4 tags unable to properly interact with the GFP 9M6 detector. It may be tempting to speculate that Myricetin because of the more extensive hydrogen bond interactions established with residues at the pocket surface, could act by clamping and rigidifying the coiled coil, which would explain the enhancement in thermal stability observed in both EBOV and MARV VP35 oligomerization domains in the presence of the compound. Conversely, because of its smaller dimension and consequently lower steric hindrance, TBBT could act by prying in a lock pick-like fashion. Future investigations are however needed to support such interpretations.

In summary, this study demonstrates that EBOV and MARV VP35 oligomerization domains are amenable targets for the development of drugs that, by altering VP35 coiled-coil conformation, will inhibit the functions for which an oligomeric VP35 is crucial, such as filoviral genome replication and innate immune evasion. The VP35 tripartite split-GFP FC system represents therefore a new promising resource in the 'antiviral research toolbox' for the identification of novel drugs that, given the high conservation degree of the VP35 oligomerization domain across all filoviruses, may be also capable of pan-filoviral activity.

Limitations to the study

The tripartite split-GFP FC system is suitable to assess the impact of mutagenesis-induced defects in the VP35 oligomer formation, and also to screen for small molecules that may affect the conformational stability of the VP35 coiled-coil, among which Myricetin and TBBT have been proven to be exemplary starting models. However, further studies are needed to evaluate their binding kinetics and inhibitory effect in the context of a full-length VP35. In fact, one limitation to this study lies in the fact that it provides insights into the oligomerization of VP35 in a domain-specific perspective, with no experiments conducted on the full-length protein in a mammalian cytoplasmic environment. Although this element could mistakenly lead to perceive the study as of limited impact, it indeed represents its point of strength. In fact, the tripartite split-GFP FC allows us to dissect out the coiled-coil mediated VP35 oligomerization from the other properties of a multifunctional and modular protein as VP35 is, whose multimerization via other domains in the full-length construct would disturb readout interpretation and inevitably mask the real potential of antiviral candidates targeting the coiled-coil mediated VP35 oligomerization, an indispensable process for the filoviral life cycle. Nevertheless, although the system can in principle be adapted to mammalian cell cultures and fluorescence imaging, it is intended to be used as an agile biochemical tool for initial screening and then to be coupled to orthogonal, well established cell-based methods such as mini-genomes or other reporter assays, as well as to experiments that use live viruses at the highest biocontainment level.

STAR★METHODS

Detailed methods are provided in the online version of this paper and include the following:

- KEY RESOURCES TABLE
- RESOURCE AVAILABILITY
  - Lead contact
  - Materials availability
  - Data and code availability
- EXPERIMENTAL MODEL AND SUBJECT DETAILS
  - Cell lines and cell cultures
- METHOD DETAILS
  - Molecular cloning, protein expression and purification
  - SEC-MALS

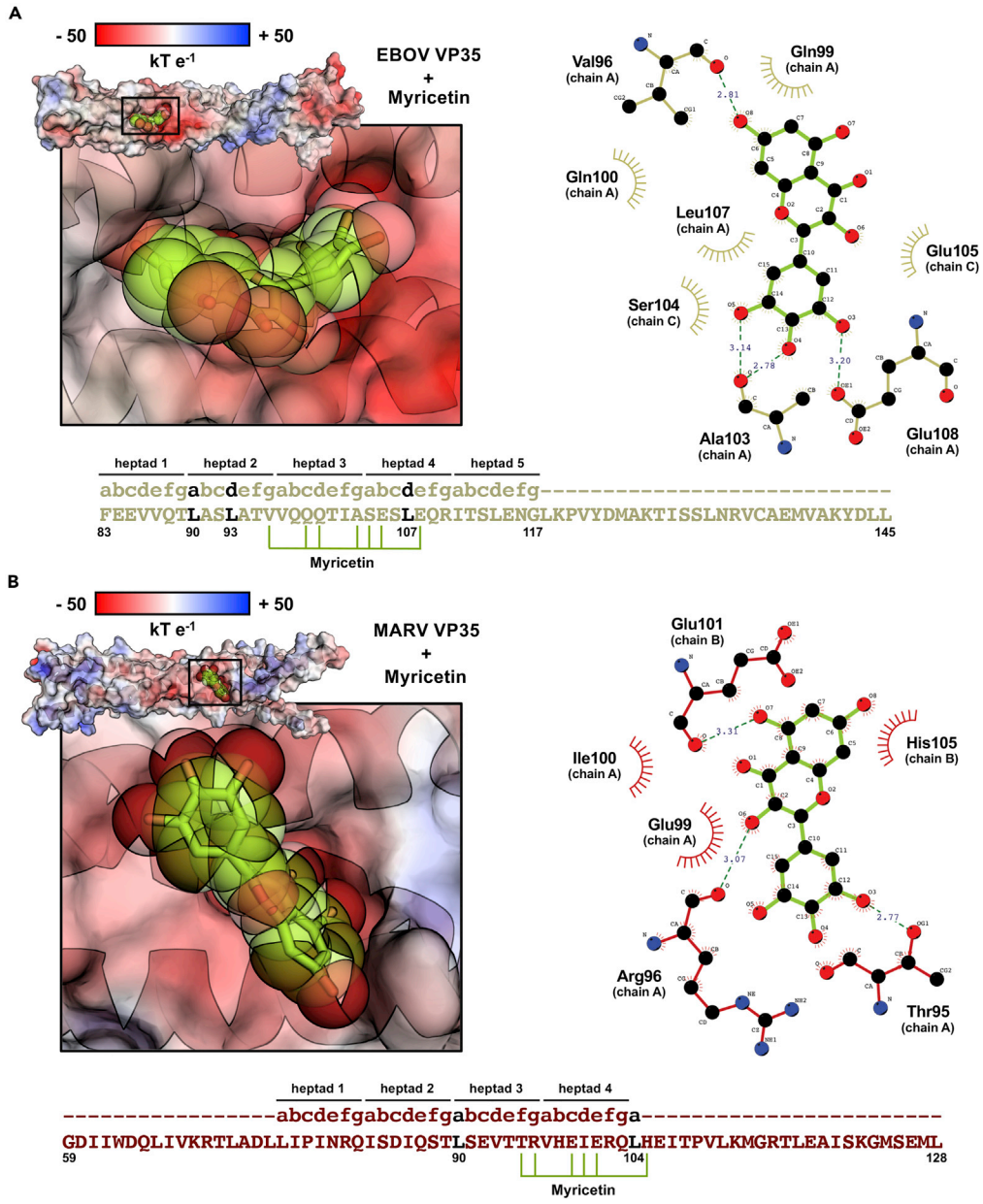

Figure 6. Molecular docking model and interaction map for Myricetin binding to EBOV and MARV VP35 oligomerization domains

(A) Cartoon representation (zoomed in the inset) of putative binding mode of Myricetin to the coiled-coil of the homo-trimeric EBOV VP35 oligomerization domain (upper left panel) and two-dimensional (2D) diagram of predicted compound-residue interactions within the binding pocket (upper right panel).

(B) Cartoon representation (zoomed in the inset) of putative binding mode of Myricetin to the coiled-coil of the homo-trimeric MARV VP35 oligomerization domain (upper left panel) and 2D diagram of predicted compound-residue interactions within the binding pocket (upper right panel). Red, white and blue regions on the VP35 isosurface represent areas of negative, neutral, and positive electrostatic surface potential, respectively (scale of −50 to +50 kT e^{-1}); H-bonds are drawn as blue dashed lines with distances between atoms indicated in angstrom (Å); hydrophobic contacts are depicted as arcs with spokes; amino acid sequences and coiled-coil heptad registers are shown below each model (lower panels), with critical Leucines at *a* and *d* positions highlighted in black, and residues interacting with Myricetin indicated by lime-green lines.

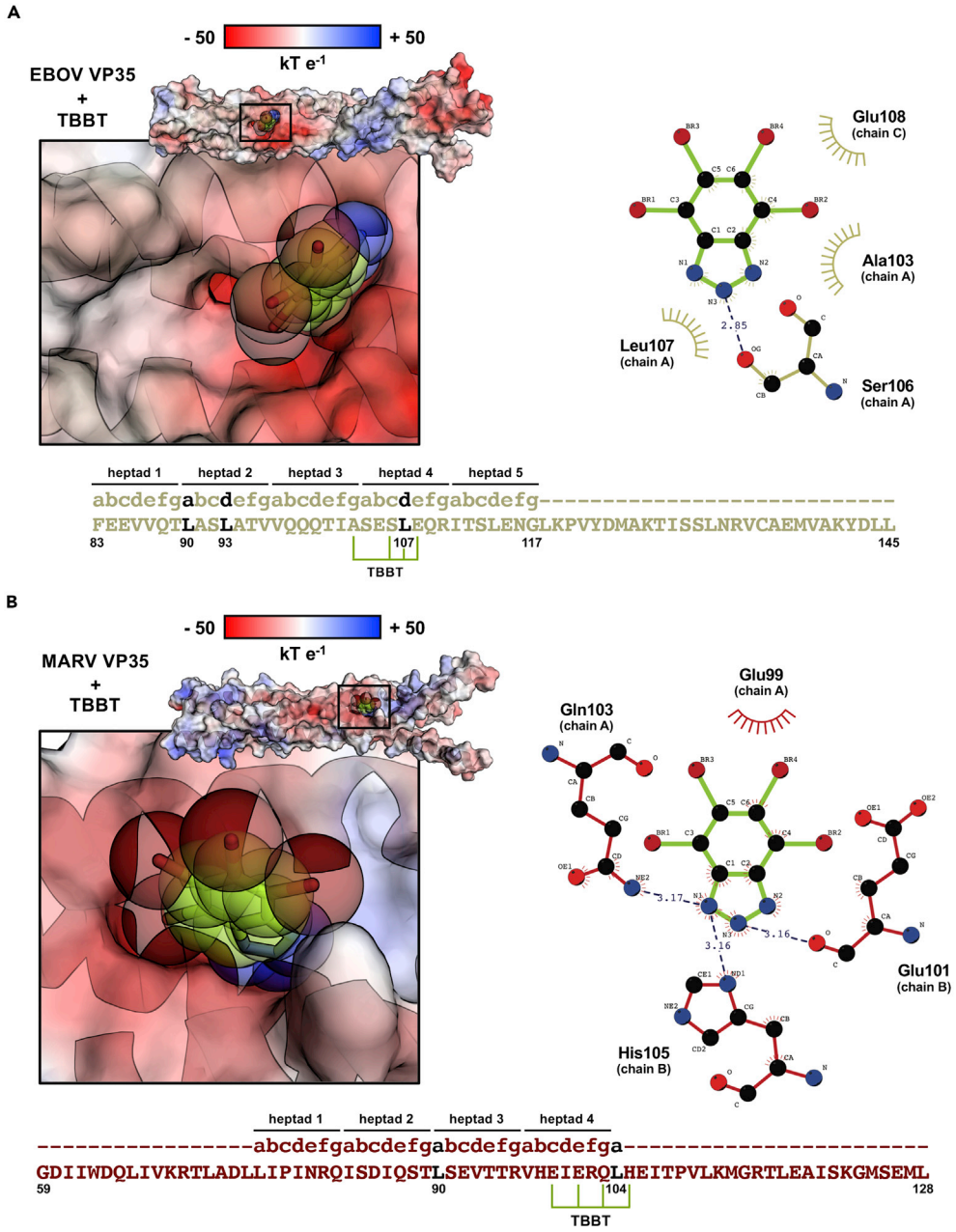

Figure 7. Molecular docking model and interaction map for TBBT binding to EBOV and MARV VP35 oligomerization domains

(A) Cartoon representation (zoomed in the inset) of putative binding mode of TBBT to the coiled-coil of the homo-trimeric EBOV VP35 oligomerization domain (upper left panel) and 2D diagram of predicted compound-residue interactions within the binding pocket (upper right panel).

(B) Cartoon representation (zoomed in the inset) of putative binding mode of TBBT to the coiled-coil of the homo-trimeric MARV VP35 oligomerization domain (upper left panel) and 2D diagram of predicted compound-residue interactions within the binding pocket (upper right panel). Red, white and blue regions on the VP35 isosurface represent areas of negative, neutral, and positive electrostatic surface potential, respectively (scale of −50 to +50 kT e^{-1}); H-bonds are drawn as blue dashed lines with distances between atoms indicated in angstrom (Å); hydrophobic contacts are depicted as arcs with spokes; amino acid sequences and coiled-coil heptad registers are shown below each model (lower panels), with critical Leucines at *a* and *d* positions highlighted in black, and residues interacting with TBBT indicated by lime-green lines.

- Far-UV CD
- Nano-DSF
- *In vivo* whole cell split-GFP FC screening
- *In vitro* split-GFP FC assay
- Homology modeling
- MD simulations
- Molecular docking
- Molecular graphics and data statistical analysis

● QUANTIFICATION AND STATISTICAL ANALYSIS

SUPPLEMENTAL INFORMATION

Supplemental information can be found online at https://doi.org/10.1016/j.isci.2022.105354.

ACKNOWLEDGMENTS

We thank colleagues at the Max-Planck Institute of Biochemistry (MPIB) and we are particularly grateful to S. Klumpe for fruitful discussion on MD simulations setups, to S. Uebel and M. Zobawa at the MPIB Bio-organic Chemistry and Biophysics Core Facility for technical support, and to M. Boicu and M. Peritore for technical assistance.

AUTHOR CONTRIBUTIONS

L.Z. conceived the study. L.Z. and I.N. designed and performed molecular cloning. L.Z., A.M.M., and C.S. performed protein expression and purification and carried out all biochemical and biophysical experiments. L.Z and M.O. performed MD simulations and molecular docking. L.Z., I.N., M.O., and A.B. performed data analysis and interpretation. W.B. supervised experimental design and data interpretation. L.Z. drafted the manuscript. All authors contributed to experimental design, data analyses and manuscript review.

DECLARATION OF INTERESTS

The authors declare no competing interests.

INCLUSION AND DIVERSITY

We support inclusive, diverse, and equitable conduct of research.

Received: May 4, 2022
Revised: September 29, 2022
Accepted: October 11, 2022
Published: November 18, 2022

REFERENCES

Baker, N.A., Sept, D., Joseph, S., Holst, M.J., and McCammon, J.A. (2001). Electrostatics of nanosystems: application to microtubules and the ribosome. Proc. Natl. Acad. Sci. USA *98*, 10037–10041. https://doi.org/10.1073/pnas.181342398.

Bale, S., Julien, J.P., Bornholdt, Z.A., Kimberlin, C.R., Halfmann, P., Zandonatti, M.A., Kunert, J., Kroon, G.J.A., Kawaoka, Y., MacRae, I.J., et al. (2012). Marburg virus VP35 can both fully coat the backbone and cap the ends of dsRNA for interferon antagonism. PLoS Pathog. *8*, e1002916. https://doi.org/10.1371/journal.ppat.1002916.

Bale, S., Julien, J.P., Bornholdt, Z.A., Krois, A.S., Wilson, I.A., and Saphire, E.O. (2013). Ebolavirus VP35 coats the backbone of double-stranded RNA for interferon antagonism. J. Virol. *87*, 10385–10388.

Borowski, P., Deinert, J., Schalinski, S., Bretner, M., Ginalski, K., Kulikowski, T., and Shugar, D. (2003). Halogenated benzimidazoles and benzotriazoles as inhibitors of the NTPase/helicase activities of hepatitis C and related viruses. Eur. J. Biochem. *270*, 1645–1653.

Bretner, M., Baier, A., Kopańska, K., Najda, A., Schoof, A., Reinholz, M., Lipniacki, A., Piasek, A., Kulikowski, T., and Borowski, P. (2005). Synthesis and biological activity of 1H-benzotriazole and 1H-benzimidazole analogues–inhibitors of the NTpase/helicase of HCV and of some related Flaviviridae. Antivir. Chem. Chemother. *16*, 315–326.

Bruhn, J.F., Kirchdoerfer, R.N., Urata, S.M., Li, S., Tickle, I.J., Bricogne, G., and Saphire, E.O. (2017). Crystal structure of the Marburg virus VP35 oligomerization domain. J. Virol. *91*, e01085-16. https://doi.org/10.1128/JVI.01085-16.

Buchan, D.W.A., and Jones, D.T. (2019). The PSIPRED protein analysis workbench: 20 years on. Nucleic Acids Res. *47*, W402–W407. https://doi.org/10.1093/nar/gkz297.

Cabantous, S., Nguyen, H.B., Pedelacq, J.D., Koraïchi, F., Chaudhary, A., Ganguly, K., Lockard, M.A., Favre, G., Terwilliger, T.C., and Waldo, G.S. (2013). A new protein-protein interaction sensor based on tripartite split-GFP association. Sci. Rep. *3*, 2854. https://doi.org/10.1038/srep02854.

Chanthamontri, C.K., Jordan, D.S., Wang, W., Wu, C., Lin, Y., Brett, T.J., Gross, M.L., and Leung, D.W. (2019). The Ebola viral protein 35 N-terminus is a parallel tetramer. Biochemistry *58*, 657–664.

Corona, A., Fanunza, E., Salata, C., Morwitzer, M.J., Distinto, S., Zinzula, L., Sanna, C., Frau, A., Daino, G.L., Quartu, M., et al. (2022). Cynarin

blocks Ebola virus replication by counteracting VP35 inhibition of interferon-beta production. Antivir. Res. *198*, 105251. https://doi.org/10.1016/j.antiviral.2022.105251.

Daino, G.L., Frau, A., Sanna, C., Rigano, D., Distinto, S., Madau, V., Esposito, F., Fanunza, E., Bianco, G., Taglialatela-Scafati, O., et al. (2018). Identification of Myricetin as an Ebola virus VP35-double-stranded RNA interaction inhibitor through a novel fluorescence-based assay. Biochemistry *57*, 6367–6378.

Di Palma, F., Daino, G.L., Ramaswamy, V.K., Corona, A., Frau, A., Fanunza, E., Vargiu, A.V., Tramontano, E., and Ruggerone, P. (2019). Relevance of Ebola virus VP35 homo-dimerization on the type I interferon cascade inhibition. Antivir. Chem. Chemother. *27*. 2040206619889220. https://doi.org/10.1177/2040206619889220.

Dolinsky, T.J., Czodrowski, P., Li, H., Nielsen, J.E., Jensen, J.H., Klebe, G., and Baker, N.A. (2007). PDB2PQR: expanding and upgrading automated preparation of biomolecular structures for molecular simulations. Nucleic Acids Res. *35*, W522–W525. https://doi.org/10.1093/nar/gkm276.

Edwards, M.R., and Basler, C.F. (2019). Current status of small molecule drug development for Ebola virus and other filoviruses. Curr. Opin. Virol. *35*, 42–56.

Greenfield, N.J. (2006). Using circular dichroism spectra to estimate protein secondary structure. Nat. Protoc. *1*, 2876–2890.

Hansen, F., Feldmann, H., and Jarvis, M.A. (2021). Targeting ebola virus replication through pharmaceutical intervention. Expert Opin. Invest. Drugs *30*, 201–226. https://doi.org/10.1080/13543784.2021.1881061.

Kandeel, M., Yamamoto, M., Al-Taher, A., Watanabe, A., Oh-Hashi, K., Park, B.K., Kwon, H.J., Inoue, J.I., and Al-Nazawi, M. (2020). Small molecule inhibitors of Middle East respiratory syndrome coronavirus fusion by targeting cavities on heptad repeat trimers. Biomol. Ther. *28*, 311–319. https://doi.org/10.4062/biomolther.2019.202.

Kim, S., Chen, J., Cheng, T., Gindulyte, A., He, J., He, S., Li, Q., Shoemaker, B.A., Thiessen, P.A., Yu, B., et al. (2021). PubChem in 2021: new data content and improved web interfaces. Nucleic Acids Res. *49*, D1388–D1395. https://doi.org/10.1093/nar/gkaa971.

Kimberlin, C.R., Bornholdt, Z.A., Li, S., Woods, V.L., Jr., MacRae, I.J., and Saphire, E.O. (2010). Ebolavirus VP35 uses a bimodal strategy to bind dsRNA for innate immune suppression. Proc. Natl. Acad. Sci. USA *107*, 314–319.

Kirchdoerfer, R.N., Abelson, D.M., Li, S., Wood, M.R., and Saphire, E.O. (2015). Assembly of the Ebola virus nucleoprotein from a chaperoned VP35 complex. Cell Rep. *12*, 140–149.

Koraïchi, F., Gence, R., Bouchenot, C., Grosjean, S., Lajoie-Mazenc, I., Favre, G., and Cabantous, S. (2018). High-content tripartite split-GFP cell-based assays to screen for modulators of small GTPase activation. J. Cell Sci. *131*, jcs210419. https://doi.org/10.1242/jcs.210419.

Kuhn, J.H., Adachi, T., Adhikari, N.K.J., Arribas, J.R., Bah, I.E., Bausch, D.G., Bhadelia, N., Borchert, M., Brantsæter, A.B., Brett-Major, D.M., et al. (2019). New filovirus disease classification and nomenclature. Nat. Rev. Microbiol. *17*, 261–263.

Kumar, P., and Woolfson, D.N. (2021). Socket2: a program for locating, visualising, and analysing coiled-coil interfaces in protein structures. Bioinformatics *37*, 4575–4577. https://doi.org/10.1093/bioinformatics/btab631.

Landeras-Bueno, S., Oda, S.I., Norris, M.J., Li Salie, Z., Guenaga, J., Wyatt, R.T., and Saphire, E.O. (2019). Sudan Ebolavirus VP35-NP crystal structure reveals a potential target for pan-Filovirus treatment. mBio *10*, e00734-19. https://doi.org/10.1128/mBio.00734-19.

Languon, S., and Quaye, O. (2019). Filovirus disease outbreaks: a chronological overview. Virology *10*. 10:1178122X19849927. https://doi.org/10.1177/1178122X19849927.

Leung, D.W., Borek, D., Luthra, P., Binning, J.M., Anantpadma, M., Liu, G., Harvey, I.B., Su, Z., Endlich-Frazier, A., Pan, J., et al. (2015). An intrinsically disordered peptide from Ebola virus VP35 controls viral RNA synthesis by modulating nucleoprotein-RNA interactions. Cell Rep. *11*, 376–389.

Leung, D.W., Ginder, N.D., Fulton, D.B., Nix, J., Basler, C.F., Honzatko, R.B., and Amarasinghe, G.K. (2009). Structure of the Ebola VP35 interferon inhibitory domain. Proc. Natl. Acad. Sci. USA *106*, 411–416.

Leung, D.W., Prins, K.C., Borek, D.M., Farahbakhsh, M., Tufariello, J.M., Ramanan, P., Nix, J.C., Helgeson, L.A., Otwinowski, Z., Honzatko, R.B., et al. (2010a). Structural basis for dsRNA recognition and interferon antagonism by Ebola VP35. Nat. Struct. Mol. Biol. *17*, 165–172.

Leung, D.W., Shabman, R.S., Farahbakhsh, M., Prins, K.C., Borek, D.M., Wang, T., Mühlberger, E., Basler, C.F., and Amarasinghe, G.K. (2010b). Structural and functional characterization of Reston Ebola virus VP35 interferon inhibitory domain. J. Mol. Biol. *399*, 347–357.

Liu, Y., Grimm, M., Dai, W.T., Hou, M.C., Xiao, Z.X., and Cao, Y. (2020). CB-Dock: a web server for cavity detection-guided protein-ligand blind docking. Acta Pharmacol. Sin. *41*, 138–144. https://doi.org/10.1038/s41401-019-0228-6.

Lupas, A.N., and Bassler, J. (2017). Coiled coils - a model system for the 21st century. Trends Biochem. Sci. *42*, 130–140.

Madeira, F., Park, Y.M., Lee, J., Buso, N., Gur, T., Madhusoodanan, N., Basutkar, P., Tivey, A.R.N., Potter, S.C., Finn, R.D., and Lopez, R. (2019). The EMBL-EBI search and sequence analysis tools APIs in 2019. Nucleic Acids Res. *47*, W636–W641. https://doi.org/10.1093/nar/gkz268.

McGee, T.D., Jr., Yi, H.A., Allen, W.J., Jacobs, A., and Rizzo, R.C. (2017). Structure-based identification of inhibitors targeting obstruction of the HIVgp41 N-heptad repeat trimer. Bioorg. Med. Chem. Lett. *27*, 3177–3184.

Meher, B.R., and Wang, Y. (2015). Exploring the drug resistance of V32I and M46L mutant HIV-1 protease to inhibitor TMC114: flap dynamics and binding mechanism. J. Mol. Graph. Model. *56*, 60–73. https://doi.org/10.1016/j.jmgm.2014.11.003.

Meng, E.C., Pettersen, E.F., Couch, G.S., Huang, C.C., and Ferrin, T.E. (2006). Tools for integrated sequence-structure analysis with UCSF Chimera. BMC Bioinf. *7*, 339. https://doi.org/10.1186/1471-2105-7-339.

Möller, P., Pariente, N., Klenk, H.D., and Becker, S. (2005). Homo-oligomerization of Marburgvirus VP35 is essential for its function in replication and transcription. J. Virol. *79*, 14876–14886.

Nguyen, H.B., Hung, L.W., Yeates, T.O., Terwilliger, T.C., and Waldo, G.S. (2013). Split green fluorescent protein as a modular binding partner for protein crystallization. Acta Crystallogr. D Biol. Crystallogr. *69*, 2513–2523.

O'Boyle, N.M., Banck, M., James, C.A., Morley, C., Vandermeersch, T., and Hutchison, G.R. (2011). Open Babel: an open chemical toolbox. J. Cheminf. *3*, 33. https://doi.org/10.1186/1758-2946-3-33.

Olejnik, J., Hume, A.J., Leung, D.W., Amarasinghe, G.K., Basler, C.F., and Mühlberger, E. (2017). Filovirus strategies to escape antiviral responses. Curr. Top. Microbiol. Immunol. *411*, 293–322.

Ortega, J.T., Parmar, T., and Jastrzebska, B. (2019). Flavonoids enhance rod opsin stability, folding, and self-association by directly binding to ligand-free opsin and modulating its conformation. J. Biol. Chem. *294*, 8101–8122. https://doi.org/10.1074/jbc.RA119.007808.

Pettersen, E.F., Goddard, T.D., Huang, C.C., Couch, G.S., Greenblatt, D.M., Meng, E.C., and Ferrin, T.E. (2004). UCSF Chimera–a visualization system for exploratory research and analysis. J. Comput. Chem. *25*, 1605–1612. https://doi.org/10.1002/jcc.20084.

Phillips, J.C., Hardy, D.J., Maia, J.D.C., Stone, J.E., Ribeiro, J.V., Bernardi, R.C., Buch, R., Fiorin, G., Hénin, J., Jiang, W., et al. (2020). Scalable molecular dynamics on CPU and GPU architectures with NAMD. J. Chem. Phys. *153*, 044130. https://doi.org/10.1063/5.0014475.

Ramanan, P., Edwards, M.R., Shabman, R.S., Leung, D.W., Endlich-Frazier, A.C., Borek, D.M., Otwinowski, Z., Liu, G., Huh, J., Basler, C.F., and Amarasinghe, G.K. (2012). Structural basis for Marburg virus VP35-mediated immune evasion mechanisms. Proc. Natl. Acad. Sci. USA *109*, 20661–20666.

Ramaswamy, V.K., Di Palma, F., Vargiu, A.V., Corona, A., Piano, D., Ruggerone, P., Zinzula, L., and Tramontano, E. (2018). Insights into the homo-oligomerization properties of N-terminal coiled-coil domain of Ebola virus VP35 protein. Virus Res. *247*, 61–70.

Reid, S.P., Cárdenas, W.B., and Basler, C.F. (2005). Homo-oligomerization facilitates the interferon-antagonist activity of the ebolavirus VP35 protein. Virology *341*, 179–189.

Ribeiro, J.V., Bernardi, R.C., Rudack, T., Stone, J.E., Phillips, J.C., Freddolino, P.L., and Schulten, K. (2016). QwikMD - integrative molecular dynamics toolkit for novices and experts. Sci. Rep. *6*, 26536. https://doi.org/10.1038/srep26536.

Roymans, D., De Bondt, H.L., Arnoult, E., Geluykens, P., Gevers, T., Van Ginderen, M., Verheyen, N., Kim, H., Willebrords, R., Bonfanti, J.F., et al. (2010). Binding of a potent small-molecule inhibitor of six-helix bundle formation requires interactions with both heptad-repeats of the RSV fusion protein. Proc. Natl. Acad. Sci. USA *107*, 308–313. https://doi.org/10.1073/pnas.0910108106.

Shu, T., Gan, T., Bai, P., Wang, X., Qian, Q., Zhou, H., Cheng, Q., Qiu, Y., Yin, L., Zhong, J., and Zhou, X. (2019). Ebola virus VP35 has novel NTPase and helicase-like activities. Nucleic Acids Res. *47*, 5837–5851. https://doi.org/10.1093/nar/gkz340.

Some, D., Amartely, H., Tsadok, A., and Lebendiker, M. (2019). Characterization of proteins by size-exclusion chromatography coupled to multi-angle light scattering (SEC-MALS). J. Vis. Exp. *148*. https://doi.org/10.3791/59615.

Trott, O., and Olson, A.J. (2010). AutoDock Vina: improving the speed and accuracy of docking with a new scoring function, efficient optimization, and multithreading. J. Comput. Chem. *31*, 455–461. https://doi.org/10.1002/jcc.21334.

Vivoli, M., Novak, H.R., Littlechild, J.A., and Harmer, N.J. (2014). Determination of protein-ligand interactions using differential scanning fluorimetry. J. Vis. Exp. *91*, 51809. https://doi.org/10.3791/51809.

Wallace, A.C., Laskowski, R.A., and Thornton, J.M. (1995). LIGPLOT: a program to generate schematic diagrams of protein-ligand interactions. Protein Eng. *8*, 127–134. https://doi.org/10.1093/protein/8.2.127.

Walshaw, J., and Woolfson, D.N. (2001). Socket: a program for identifying and analyzing coiled-coil motifs within protein structures. J. Mol. Biol. *307*, 1427–1450. https://doi.org/10.1006/jmbi.2001.4545.

Webb, B., and Sali, A. (2016). Comparative protein structure modeling using MODELLER. Curr. Protoc. Bioinf. *54*, 5.6.1–5.6.37. https://doi.org/10.1002/cpbi.3.

Williams, C.J., Headd, J.J., Moriarty, N.W., Prisant, M.G., Videau, L.L., Deis, L.N., Verma, V., Keedy, D.A., Hintze, B.J., Chen, V.B., et al. (2018). MolProbity: more and better reference data for improved all-atom structure validation. Protein Sci. *27*, 293–315. https://doi.org/10.1002/pro.3330.

Yang, Y., Shin, J.Y., Oh, J.M., Jung, C.H., Hwang, Y., Kim, S., Kim, J.S., Yoon, K.J., Ryu, J.Y., Shin, J., et al. (2010). Dissection of SNARE-driven membrane fusion and neuroexocytosis by wedging small hydrophobic molecules into the SNARE zipper. Proc. Natl. Acad. Sci. USA *107*, 22145–22150.

Zhang, J.H., Chung, T.D., and Oldenburg, K.R. (1999). A simple statistical parameter for use in evaluation and validation of high throughput screening assays. J. Biomol. Screen *4*, 67–73.

Zhang, Y., and Skolnick, J. (2005). TM-align: a protein structure alignment algorithm based on the TM-score. Nucleic Acids Res. *33*, 2302–2309. https://doi.org/10.1093/nar/gki524.

Zhu, T., Song, H., Peng, R., Shi, Y., Qi, J., and Gao, G.F. (2017). Crystal structure of the Marburg virus nucleoprotein core domain chaperoned by a VP35 peptide reveals a conserved drug target for Filovirus. J. Virol. *91*, e00996-17. https://doi.org/10.1128/JVI.00996-17.

Zinzula, L., Esposito, F., Mühlberger, E., Trunschke, M., Conrad, D., Piano, D., and Tramontano, E. (2009). Purification and functional characterization of the full length recombinant Ebola virus VP35 protein expressed in E. coli. Protein Expr. Purif. *66*, 113–119.

Zinzula, L., Esposito, F., Pala, D., and Tramontano, E. (2012). dsRNA binding characterization of full length recombinant wild type and mutants Zaire ebolavirus VP35. Antivir. Res. *93*, 354–363.

Zinzula, L., Nagy, I., Orsini, M., Weyher-Stingl, E., Bracher, A., and Baumeister, W. (2019). Structures of Ebola and reston virus VP35 oligomerization domains and comparative biophysical characterization in all Ebolavirus species. Structure *27*, 39–54.e6.

STAR★METHODS

KEY RESOURCES TABLE

REAGENT or RESOURCE	SOURCE	IDENTIFIER
Bacterial and virus strains		
E. coli NEB® 5-alpha	New England BioLabs	Cat #C2987H
E. coli BL21 (DE3)	New England BioLabs	Cat #C25271
Chemicals, peptides, and recombinant proteins		
LB Broth (Miller)	Carl-Roth	Cat #X968.4
Agar-Agar, bacteriological	Carl-Roth	Cat #2266.1
di-Potassium hydrogen phosphate trihydrate	Carl-Roth	Cat #6878.1
Potassium dihydrogen phosphate	Carl-Roth	Cat #3904.1
Sodium dihydrogen phosphate dihydrate	Carl-Roth	Cat #T879.1
di-Sodium hydrogen phosphate dihydrate	Carl-Roth	Cat #4984.3
Sodium chloride	Sigma-Aldrich	Cat #S3014
Ampicillin sodium Salt	Sigma-Aldrich	Cat #A9518
Kanamycin sulfate	SERVA	Cat #26899.03
Spectinomycin sulfate	Enzo Life Sciences	Cat #BML-A281-0010
IPTG	Carl-Roth	Cat #CN08.4
Glycerol	Sigma-Aldrich	Cat #G5516
Imidazole	Merck	Cat #1047160250
Lysozyme from chicken egg white powder	Sigma-Aldrich	Cat #62971
cOmplete EDTA-free Protease Inhibitor Cocktail	Roche	Cat #11873580001
DNase I from bovine pancreas	Roche	Cat #10104159001
TCEP	TRC Canada	Cat #T012500
Trizma®-hydrochloride	Sigma-Aldrich	Cat #93363
Magnesium chloride	Sigma-Aldrich	Cat #M8266
Cerivastatin sodium salt hydrated ≥98%	Sigma-Aldrich	Cat #SML0005
Cynarin ≥98%	Supelco	Cat #91801
Ivermectin ≥98%	Sigma-Aldrich	Cat #I8898
Myricetin ≥96%	Sigma-Aldrich	Cat #M6770
Prasugrel ≥98%	Sigma-Aldrich	Cat #SML0331
Suramin Sodium salt ≥98%	Sigma-Aldrich	Cat #S2671
TBBT ≥98%	Sigma-Aldrich	Cat #T0826
TMC353121 ≥ 98%	MedChemExpress	Cat #HY-11097
eGFP	This work	N/A
BSA	ThermoFisher	Cat #AM2616
NuPAGE™ 4–12% Bis-Tris protein gels	ThermoFisher	Cat #NP0232
NuPAGE™ LDS Sample Buffer	ThermoFisher	Cat #NP0007
NuPAGE™ Antioxidant	ThermoFisher	Cat #NP0005
NuPAGE™ Sample Reducing Agent	ThermoFisher	Cat #NP0004
NuPAGE™ MES SDS Running Buffer	ThermoFisher	Cat #NP0002
PageRuler™ Prestained Protein Ladder	ThermoFisher	Cat #26616
Recombinant DNA		
pET-21b (+) DNA-Novagen	Merck Millipore	Cat #69741
pETDuet-1 DNA-Novagen	Merck Millipore	Cat #71146

(*Continued on next page*)

Continued

REAGENT or RESOURCE	SOURCE	IDENTIFIER
pRSFDuet-1 DNA-Novagen	Merck Millipore	Cat #71341
pCDFDuet-1 DNA-Novagen	Merck Millipore	Cat #71340
pET-21b-EBOV-VP35(75–185)	This work	N/A
pET-21b-MARV-VP35(58–174)	This work	N/A
pETDuet-GFP-9M6	This work	N/A
pRSFDuet-GFP-10M2-EBOV-VP35(75–185) WT	This work	N/A
pCDFDuet-GFP-11M4-EBOV-VP35(75–185) WT	This work	N/A
pRSFDuet-GFP-10M2-EBOV-VP35(75–185) L90A/L93A/L107A	This work	N/A
pCDFDuet-GFP-11M4-EBOV-VP35(75–185) L90A/L93A/L107A	This work	N/A
pRSFDuet-GFP-10M2-MARV-VP35(85–174) WT	This work	N/A
pCDFDuet-GFP-11M4-MARV-VP35(58–174) WT	This work	N/A
pRSFDuet-GFP-10M2-MARV-VP35(58–174) L90A/L104A	This work	N/A
pCDFDuet-GFP-11M4-MARV-VP35(58–174) L90A/L104A	This work	N/A
Deposited data		
Crystal Structure of Split GFP complexed with engineered sfCherry with an insertion of GFP fragment	Nguyen et al., 2013	PDB: 4KF5
Crystal structure of the oligomerization domain of Vp35 from Ebola virus	Zinzula et al., 2019	PDB: 6GBO
Crystal structure of the Marburg Virus VP35 Oligomerization Domain P4222	Bruhn et al., 2017	PDB: 5TOI
Software and algorithms		
PSIPRED	Buchan and Jones, 2019	http://bioinf.cs.ucl.ac.uk/psipred/
ASTRA 6	Wyatt Technology	https://www.wyatt.com/products/software/astra.html
Spectra Manager	Jasco	https://www.jasco.de/Spectroscopy/Software
PR.ThermControl	NanoTemper Technologies	https://nanotempertech.com/prometheus-pr-thermcontrol-software/
QuestGraph™ IC_{50} calculator	AAT Bioquest	https://www.aatbio.com/tools/ic50-calculator
Clustal Omega	Madeira et al., 2019	https://www.ebi.ac.uk/Tools/msa/clustalo/
MODELLER 10.1	Webb and Sali, 2016	https://salilab.org/modeller/
MolProbity	Williams et al., 2018	http://molprobity.biochem.duke.edu
SOCKET	Walshaw and Woolfson, 2001	http://coiledcoils.chm.bris.ac.uk/socket/server.html
QwikMD	Ribeiro et al., 2016	http://www.ks.uiuc.edu/Research/qwikmd/
NAMD	Phillips et al., 2020	https://www.ks.uiuc.edu/Research/namd/
SOCKET2	Kumar and Woolfson, 2021	http://coiledcoils.chm.bris.ac.uk/socket2/home.html

(*Continued on next page*)

Continued

REAGENT or RESOURCE	SOURCE	IDENTIFIER
PubChem	Kim et al., 2021	https://pubchem.ncbi.nlm.nih.gov
Open Babel	O'Boyle et al., 2011	http://openbabel.org/wiki/Main_Page
AutoDock Vina	Trott and Olson, 2010	https://vina.scripps.edu
CB-Dock	Liu et al., 2020	http://clab.labshare.cn/cb-dock/php/index.php
LIGPLOT	Wallace et al., 1995	https://www.ebi.ac.uk/thornton-srv/software/LIGPLOT/
Chimera	Pettersen et al., 2004	https://www.cgl.ucsf.edu/chimera/
PyMOL	Schrödinger	http://www.pymol.org/
Tm-align	Zhang and Skolnick, 2005	https://zhanglab.ccmb.med.umich.edu/TM-align/
MatchMaker	Meng et al., 2006	https://www.cgl.ucsf.edu/chimera/docs/ContributedSoftware/matchmaker/matchmaker.html
PDB2PQR	Dolinsky et al., 2007	https://www.poissonboltzmann.org
APBS	Baker et al., 2001	https://www.poissonboltzmann.org
ChemDraw	PerkinElmer	https://perkinelmerinformatics.com/products/research/chemdraw
MolView	MolView	https://molview.org
Prism 9	GraphPad	https://www.graphpad.com
Other		
HisTrap FF crude 1mL	GE Healthcare	Cat #11-004-58
Superose 12 10/300 GL	GE Healthcare	Cat #17-5173-01
Superdex 200 10/300 GL	GE Healthcare	Cat #17-5175-01
Precision cuvette highly pure quartz glass Suprasil™ 110-QS	Hellma	Cat #110-1-40
Prometheus NT.48 Series nanoDSF Grade NanoTemper Standard Capillaries	NanoTemper Technologies	Cat #PRC002
96-well Black Flat Bottom Polystyrene NBS Microplate	Corning	Cat #3991
384-well Low Flange Black Flat Bottom Polystyrene NBS Microplate	Corning	Cat #3375

RESOURCE AVAILABILITY

Lead contact

Further information and requests for resources and reagents should be directed to and will be fulfilled by the lead contact, Luca Zinzula (zinzula@biochem.mpg.de).

Materials availability

The plasmids and cell lines generated in this study are available from the lead contact and will be subjected to a material transfer agreement.

Data and code availability

The datasets generated in this study are available from the lead contact on reasonable request. This paper does not report original code.

EXPERIMENTAL MODEL AND SUBJECT DETAILS

Cell lines and cell cultures

Chemically-competent *E. coli* NEB® 5-alpha and BL21-DE3 cells were purchased from New England Biolabs, transformed with the corresponding plasmids, cultured in Luria-Bertani (LB) and Terrific broth (TB) medium, respectively, and supplemented with 15% Glycerol for long-term storage at – 80°C.

METHOD DETAILS

Molecular cloning, protein expression and purification

Boundaries of EBOV and MARV VP35 oligomerization domains were designed after secondary structure prediction using the PSIPRED (Buchan and Jones, 2019) server. Codon-optimized cDNAs encoding for WT and mutant L90A/L93A/L107A EBOV (*Zaire ebolavirus*, Yambuku-Mayinga, GenBank: NC_002549.1, residues 75–185) and WT and mutant L90A/L104A MARV (*Marburg marburgvirus*, Elgon-Musoke, GenBank: NC_001608.3, residues 58–174) VP35 oligomerization domains, native or N-terminally fused to GFP beta-strands 10 and 11 and for GFP beta-strands 1–9 (PDB: 4KF5, chain C and A, respectively) (Nguyen et al., 2013) were all obtained by custom synthesis (Eurofins Genomics), cloned into modified pET-21b, pRSFDuet, pCDFDuet and pETDuet plasmid vectors (Novagen), respectively, and propagated ot maintained for long-term storage upon transformation of chemically competent *E. coli* NEB® 5-alpha (New England Biolabs) cells. Recombinant His6-tagged proteins were expressed or co-expressed in *E. coli* BL21-DE3 (New England Biolabs) cells grown in TB medium supplemented with 50mgmL^{-1} Kanamycin and/or 50mgmL^{-1} Spectinomycin and/or 100mgmL^{-1} Ampicillin at 37°C to an OD 600 nm of 0.8, upon induction with 0.65–0.75 mM isopropyl-b-D-1-thiogalactopyranoside (IPTG) overnight (ON) at 25°C. Harvested cells were lysed in buffer A (50 mM sodium phosphate, pH 8.0; 500 mM NaCl; 5% (v/v) glycerol; 20 mM imidazole) supplemented with 1 mg mL-1 Lysozyme (Sigma-Aldrich), cOmplete EDTA-free Protease Inhibitor Cocktail (Roche) and DNase I (Roche), then sonicated and centrifuged at 30,000gat 4°C for 30 min. The supernatant was loaded onto a 1 mL HisTrap FF crude (GE Healthcare) column equilibrated in buffer A and connected to an ÄKTA™ pure FPLC system (GE Healthcare). Column washing and protein elution were performed in buffer A containing 40 mM and 900 mM imidazole, respectively. SEC was performed on a Superose 12 10/300 GL (GE Healthcare) column in buffer B (25 mM Tris-HCl, pH 8.0; 150 mM NaCl; 0.2 mM $MgCl_2$) connected to an ÄKTA™ pure FPLC system (GE Healthcare). Protein purity and homogeneity were assessed by 4–12% NuPAGE SDS-PAGE (ThermoFisher). Protein identities and integrity were confirmed by WB and LC/MS. Purified full-length recombinant eGFP was kindly provided by the Protein Production Core Facility of the Max-Planck Institute of Biochemistry (Martinsried, Germany).

SEC-MALS

SEC-purified main peak fractions of co-expressed protein samples (0.5 mg) were loaded on a Superdex 200 10/300 GL (GE Healthcare) column connected to a 1100 series HPLC system (Agilent Technologies), with its variable UV absorbance detector set to 280 nm and coupled in line to a mini DAWN TREOS MALS detector followed by an Optilab rEX refractive-index detector (Wyatt Technology, 690 nm laser) (Some et al., 2019). Runs were performed at 23°C and 0.75mLmin^{-1} flow rate in buffer B supplemented with 1 mM tris(2-carboxyethyl)-phosphine (TRC Canada). Absolute molecular mass was calculated by using bovine serum albumin (BSA) (ThermoFisher) as calibration standard and the ASTRA 6 software (Wyatt Technology) with the dn/dc value set to 0.185mLg^{-1}.

Far-UV CD

CD measurements were recorded on a J-715 spectropolarimeter equipped with a PDF 3505 Peltier thermostat (Jasco) using a high-precision quartz cuvette of 1-mm path length (Hellma). Protein samples were analyzed at 0.1mgmL^{-1} in buffer B. Spectra were recorded averages of four accumulations in the 195–250 nm wavelength range, at 23°C, 50nmmin^{-1} scanning speed and 1 s response time. Mean molar per residue ellipticity (MRE) was calculated according to MRE as equal to 3300 $m\ DA\ (l\ c\ n)^{-1}$, where m is the molecular mass in Dalton, A is the Absorbance, l is the pathlength in cm, n the residue number, and c the protein concentration in mg mL^{-1} (Greenfield, 2006). Data were processed by using the Spectra Manager software (Jasco), the CONTINLL deconvolution method and the SMP56 reference set to estimate protein α-helical content.

Nano-DSF

For thermal unfolding profiles, protein samples were diluted to 3.0–4.5mgmL^{-1} in buffer B, loaded on standard capillaries and subjected to a linear 20–95°C thermal gradient at 0.5°C min^{-1} rate using a Prometheus NT.48 Nano-DSF instrument (NanoTemper Technologies). The temperature-dependent shift in intrinsic fluorescence at emission wavelengths of 330 and 350 nm was measured, and inflection points of fluorescence transition corresponding to the Tm values were determined as the first derivative maxima of the fluorescence intensities ratio at the measured wavelengths (F330/F350). Protein-ligand interaction studies were performed as described by Vivoli and colleagues (Vivoli et al., 2014). Myricetin (≥96%,

Sigma-Aldrich) and TBBT (≥98%, Sigma-Aldrich) were tested at fixed concentration in excess (100 μM C_f) or equal to the IC_{50} value obtained in the *in vitro* split-GFP FC assay, and against a fixed amount of protein. After incubation of 60minat RT, sample quadruplicates or triplicates were tested and Tm values were averaged from at least three independent measurements, then processed using the PR.ThermControl software (NanoTemper Technologies).

In vivo whole cell split-GFP FC screening

Transformed *E. coli* BL21 (DE3) cells, co-expressing WT and mutant EBOV or MARV GFP 10M2/11M4 VP35 oligomerization domains and GFP 9M6, or singly expressing each component of the tripartite system, the full length eGFP or untagged VP35 oligomerization domains as positive and negative controls, respectively, were grown to saturation at 37°C ON in LB medium supplemented with the appropriate combination of antibiotics. After induction with 1 mM IPTG, an aliquot (50–100 μL) of each ON culture was seeded on LB agar plates containing the same antibiotic combination and 0.75 mM IPTG, and incubated at 37°C for 24 h. Induced colonies on plates were screened for fluorescence intensity and imaged on an iBright FL1500 imaging system (ThermoFisher Scientific) set to green LED (470–550 nm) transillumination and 0.11 s exposure time.

In vitro split-GFP FC assay

Reactions were set up as quadruplicates or triplicates in 100 μL or 50 μL volume in buffer B on 96 or 384-well low-flange, black flat bottom microplates (Corning), respectively. WT and mutant EBOV and MARV GFP 10M2, 11M4 or GFP 10M2/11M4 VP35 oligomerization domains at 2.3 μM final concentration (C_f) were tested singly or mixed with an excess of GFP 9M6 (C_f of 10 μM for initial read-out screening), ranging from 36.8 μM to 0.575 μM C_f for determination of the optimal 9M6:10M2-11M4 ratio and equal to 9.2 μM C_f in all subsequent experiments, respectively. Reactions were incubated on a THERMOstar orbital shaker (BMG LabTech) set to 300 rpm, for 15–240minat 4°C, 23°C and 37°C for determination of the optimal incubation time and temperature, and for 60minat 23°C in all subsequent experiments, respectively. The fluorescence signal was measured as the average of total counts (subtracting the background fluorescence of buffer B as blank) using a Synergy HTX Multi-Mode microplate reader (Bio-Tek) equipped with filters for 485 and 528 nm excitation and emission wavelengths, respectively. Full-length eGFP and GFP 9M6 complemented with GFP 10M2/11M4 of WT EBOV and MARV VP35 oligomerization domains were used as standard and positive controls, respectively. GFP 9M6 complemented with GFP 10M2/11M4 L90A/L93A/L107A EBOV and L90A/L104A MARV VP35 oligomerization domains, GFP 9M6, GFP 10M2- and GFP11M4-fused, as well as native WT and mutant EBOV and MARV VP35 oligomerization domains were all used as negative controls. The *Z′* factor was calculated as described by Zhang et al. (1999), as Z' equal to $1–3[(SD_s + SD_b)/(M_s + M_b)]$, where SD_s is the standard deviation of the positive control signal, SD_b is the standard deviation of the negative control background, M_s is the mean of the positive control signal, and M_b is the mean of the negative control background (Zhang et al., 1999). For antiviral screening validation, a pilot set of compounds including Cerivastatin, Ivermectin, Prasugrel, Suramin, TBBT (≥98%, Sigma-Aldrich), Cynarin (≥98%, Supelco), Myricetin (≥96%, Sigma-Aldrich) and TMC353121 (≥98%, MedChemExpress) was tested by incubating each of those alone or in the presence of full-length eGFP, or pre-incubating each of those with GFP 10M2/11M4 VP35, for 60minat 23°C. Initial test was performed at 100 μM C_f under the determined optimal assay parameters, then positive hits Myricetin and TBBT were tested at increasing concentrations ranging from 0.16 μM to 2500 μM C_f. After further incubation with GFP 9M6, fluorescence counts were measured and plotted as percentages of positive control. A non-linear regression fitting model was applied to the raw experimental data and IC_{50} values were determined with the QuestGraph™ (AAT Bioquest) IC_{50} calculator server (https://www.aatbio.com/tools/ic50-calculator).

Homology modeling

Homology models of putative tetrameric EBOV VP35 (WT and L90A/L93A/L107A mutant) and MARV VP35 (WT and L90A/L104A mutant) oligomerization domains were generated by using the RESTV VP35 ortholog as template (PDB: 6GBQ) (Zinzula et al., 2019). Pairwise sequence alignment was generated by using Clustal Omega (Madeira et al., 2019), visually inspected and fed into MODELLER 10.1 (Webb and Sali, 2016) for model building using the *model-multichain.py* routine. For each construct the final structure was selected from an output of thirty models based on the MODELLER objective function. Ramachandran plot and evaluation of side chains clashes evaluation were calculated using the MolProbity (Williams et al., 2018) web server.

MD simulations

Coiled-coil boundaries in the solved homo-trimeric EBOV (PDB: 6GBO, residues 83–117) (Zinzula et al., 2019) and MARV (PDB: 5TOI, residues 78–109) (Bruhn et al., 2017) VP35 oligomerization domains, as well as in their homology-modelled homo-tetrameric versions, were defined using the SOCKET (Walshaw and Woolfson, 2001) software. For the WT and as well as *in silico* generated L90A/L93A/L107A and L90A/L104A mutants, coiled-coils were prepared for the MD runs using QwikMD (Ribeiro et al., 2016) software. Systems were solvated in a 0.15 M NaCl water box, then energy-minimized, equilibrated and subjected to all-atoms production simulations of 200 ns at 37°C using the NAMD (Phillips et al., 2020) software. Trajectories were analyzed by the QwikMD (Ribeiro et al., 2016) software. Evaluation of fluctuating residues between WT and mutant VP35 coiled-coils was performed considering as threshold the cut off value in the difference of root-mean-squared fluctuation (ΔRMSF) of $\pm$0.5 Å, as previously described (Meher and Wang, 2015). Post-simulation analysis of coiled-coil conformation and register, knobs-into-holes packing and inter-helix and knobs angles was performed using SOCKET2 server (Kumar and Woolfson, 2021).

Molecular docking

Myricetin (CID: 5281672) and TBBT (CID: 1694) atomic coordinates were retrieved from PubChem (Kim et al., 2021) as SDF files and converted to PDB format by using Open Babel web server (O'Boyle et al., 2011). Blind docking experiments of both ligands on the solved trimeric EBOV (PDB: 6GBO) (Zinzula et al., 2019) and MARV (PDB: 5TOI) (Bruhn et al., 2017) VP35 oligomerization domains, as well as on their respective tetrameric homology models, were performed by using the AutoDock Vina algorithm (Trott and Olson, 2010) on the CB-Dock (Liu et al., 2020) web server. Vina score, cavity size, docking center and size of predicted cavity parameters were all set to default values. Best poses were selected and analyzed for bi-dimensional visualization of residue-ligand interactions, using the LIGPLOT software (Wallace et al., 1995).

Molecular graphics and data statistical analysis

Structural alignments, superpositions and depictions of proteins and ligands were produced with the Chimera v.1.13.1 (Pettersen et al., 2004) and PyMOL v.2.4 software (http://www.pymol.org/). Structural comparison between WT and mutant EBOV and MARV VP35 coiled-coils was performed by using TM-align (Zhang and Skolnick, 2005) and the MatchMaker (Meng et al., 2006) tools as implemented in the Chimera software (Pettersen et al., 2004). Poisson–Boltzmann electrostatic surface potential was calculated with the PARSE force field in PDB2PQR (Dolinsky et al., 2007) and APBS (Baker et al., 2001) as implemented in the PyMOL software (http://www.pymol.org/). Chemical structures of ligands were produced with the ChemDraw software (PerkinElmer) and the MolView server (https://molview.org).

QUANTIFICATION AND STATISTICAL ANALYSIS

Plotting and analysis of experimental data was done by use of the Prism 9 software (GraphPad). Data points and standard errors refer to averages (mean, SD) of replicates from at least three independent experiments.